Hochschule
Bonn-Rhein-Sieg
University of Applied Sciences

Deutsches Zentrum
für Luft- und Raumfahrt
German Aerospace Center

Master's Thesis

Automatic Defect Detection for Selective Laser Melting using Machine Learning

submitted to the

Department of Electrical Engineering, Mechanical Engineering and Technical Journalism

in partial fulfillment of the requirements for the degree

Master of Engineering

in

Mechanical Engineering - Virtual Product Development

by

Philipp Rosauer
ID: 9029367

December 2020

Examiner:	Dr. Jan Kleinert
Second Examiner:	Prof. Corinna Thomser

Contents

List of Figures

List of Abbreviations

AM	Additive Manufacturing
CAD	Computer Aided Design
CNN	Convolutional Neural Network
CT	Computer Tomography
IOU	Intersection Over Union
mAP	Mean Average Precision
ML	Machine Learning
MPM	Melt Pool Monitoring
ReLU	Rectified Linear Unit
SLM	Selective Laser Melting
SLS	Selective Laser Sintering
SM	Smart Manufacturing
YOLO	You Only Look Once

1 Introduction and Motivation

Quality assurance is a very crucial task in production, especially in the case of safety-relevant components, whose failure can have catastrophic consequences.

1.1 Motivation

The development of more accurate sensors, gathering more data in all sorts of processes, already shown a significant impact on development, production and deployment of materials, components, tools and machines in various industries. This inevitably results in a steady increase in the amount of available data, which becomes more and more difficult to process with conventional techniques. However, advances in information technologies and especially in rather new fields such as Big Data and Machine Learning (ML) offer the potential to truly transform manufacturing approaches [8, 44]. Terms such as Industrie 4.0, Smart Manufacturing (SM), Digital Twin or Smart Factory and their increasing use in media and politics demonstrate the significance of these transformative developments.
At the same time new manufacturing processes, first and foremost Additive Manufacturing (AM), are pushing into ever new industries and applications with no less disruptive innovations. Initially used primarily in the processing of plastics, more and more techniques have been developed in recent years to process an ever-growing variety of materials [43].
According to Wuest et al. [44] the key challenges of manufacturing today are sustainability; adoption and utilization of new technologies in both manufacturing and information management; agility, flexibility and innovation in supply chains, services, products and management; as well as collaboration between industry and research. The combination of both SM and AM offer a unique possibility to face all of these challenges simultaneously. While flexibility and agility in development and manufacturing processes is a key advantage of AM over conventional manufacturing, process monitoring and SM in general already offer various solutions to further increase efficiency not only in production, but also supply chain management or servicing. However, process monitoring of AM techniques is a rather new field of study and requires knowledge and expertise of both smart and additive manufacturing.
Selective Laser Melting (SLM) is one of the most prominent metalworking AM techniques, in which components are produced layer by layer with a laser source melting a metal powder. Research has proven the capability of this process to produce strong and highly dense, as well as porous, very light structures. Currently, these component properties are achieved by post-process analysis of manufactured components and pre-process parameter variation. While offering a wide range of advantages, SLM is a rather complex process with a great amount of parameters influencing the component quality. Ongoing research is focused mainly on new parameter combinations and better isolation of the process from the environment to improve

process stability. Furthermore, process monitoring is playing an increasingly important role to both better understand the process and to optimize its variable parameters. More recent developments in industry and research facilities showed the potential of the gathered data in order to assure component quality in-situ by controlling process parameters accordingly. To achieve this goal of a feedback-loop to control parameters without user input and reduce the need of costly post-process analysis, a system is needed that can detect potential errors during manufacturing and understand how to adjust parameters to prevent defect formation.

1.2 Aim

To investigate how such errors, or material defects, occurring during production can be automatically detected with the use of state of the art ML algorithms is the aim of this thesis.
This aim can be subdivided into multiple tasks that need to be addressed in order to achieve it. The first task is to research what kind of defects occur during production and what causes them. Then an approach needs to be found how these defects could be detected during manufacturing. In this decision process limitations of available hardware need to be considered. Once it is understood what kind of defects are to be detected and how their emergence is observed as specific events, another decision has to be made how to process the gathered data. And finally the task of automatic detection of events attributed to the presence of defects needs to be solved.
These steps result in a workflow that is implemented as a prototype. Furthermore, the applicability and performance of this elaborated workflow or concept is investigated. To do so, it is extended by the steps of sample planning and production. The samples produced must be designed in such a way that they allow the workflow to be checked as realistically as possible.
In summary, a workflow is elaborated and implemented to investigate the performance of a developed concept to automatically detect defects in selective laser molten parts.

1.3 Outline

This thesis is divided into four parts: State of the Art, Methodology, Results and Discussion and Conclusion and Outlook.
In the first part the general concept of both AM and ML is presented and SLM and Neural Networks are introduced in greater detail. The focus in the description of SLM is on the formation of defects. In addition, methods are presented with which the reduction of such defects is attempted. In particular, different approaches to process monitoring are presented. Furthermore, an overview of previous research is given, which deal with the use of ML in AM and in particular SLM.
The second part of this thesis deals with the elaboration of a workflow to perform the specified tasks. The steps of this workflow are explained and decisions about selected methods are justified. First, the use of the selected ML algorithm is motivated and its operation and implementation is explained. Then, the task of data generation and collection is addressed by presenting the design of specially manufactured samples. Furthermore the entire process of

build preparation, necessary for production and influencing later collected results, is described and the parameter choice of the production process is justified. Also, the data processing and preparation to convert the measured data in a format that meets the requirements of the selected ML algorithm is explained and chosen processing parameters are justified. Then, the application of the chosen ML algorithm and all necessary steps are described. Finally, some methods of conventional data analysis are presented, which are used to asses the overall process as well as some specific steps, such as manufacturing quality or data preparation.
The results of some scenarios, compiled to check the performance of the workflow, are presented and discussed in the third part of this work. For this, mainly three data sets are composed, containing different parts of the gathered data. Each composed data set is described, analyzed with conventional analysis methods and fed into the ML algorithm. The performance of the algorithm is discussed for each data set which are further divided into subsets to analyze specific behavior. The third data set is specifically composed to further analyze the performance of the manufacturing and data preparation process. For this, the influence of two factors is analyzed in greater detail. This third section closes with a brief evaluation of the developed workflow based on the gained experience.
The final part of this thesis concludes the discussed results and provides an outlook for future research. This outlook is divided into a data section, providing ideas regarding the collection of more data to further investigate the presented methods, a workflow section, in which improvements of the structure and implementation are recommended. Also, further research of the SLM process is derived from the findings presented in this work and lastly the improvement of the ML algorithm and its implementation is suggested and further research using completely different algorithms resulting in new workflow architectures is recommended.

2 State of the Art

Both, AM and ML are relatively young research fields. The anticipated great potentials of both methods lead to broad and vivid research across many fields of study, some of which are presented in the following.

2.1 Additive Manufacturing

Often referred to as 3D-printing, AM offers a variety of advantages, such as functional integration, weight reduction, part customization and increased sustainability over conventional manufacturing techniques [12, 17, 38, 27]. At first, AM was primarily used for rapid prototyping and the accessibility of the technology lead to a broad popularity far beyond industry and research. One of the first AM techniques developed, is the Fused Deposition Modeling of continuous thermoplastic filament, still being one of the most popular AM techniques [39]. With the introduction of AM of metal alloys, new processes opened up possibilities beyond the product development phase. Developments in crucial fields like lasers, Computer Aided Design (CAD), -Engineering and -Manufacturing accelerated AM technologies in the early 2000s [46]. The first metal AM techniques, like Selective Laser Sintering (SLS) , only produced green bodies, which then needed heat treatment to form a solid metal structure. Further developments allowed higher energy input and with that direct melting of metal powder, eliminating the step of firing. Today SLM, also called Laser Powder Bed Fusion, is the most common AM technique for processing metal alloys [43]. The advance of SLM is due to its capability of producing components with properties, like ultimate tensile strength, relative density or surface roughness, close to or even outperforming conventional manufacturing [33]. The recently presented production systems, developed for serial production, such as the NXG XII 600 by *SLM Solutions*, show that AM is on the verge of becoming an integral part of production.
Moreover, SLM offers the possibility to process a wide range of metal alloys, such as Aluminum (AlSi10Mg), Cobalt (CoCr28Mo6), Nickel (IN625), Iron (316L), Copper (CuNi2SiCr) and Titanium (Ti6Al4V) alloys and in theory, is capable of processing every weldable metal alloy [48]. However, to produce components of highest quality, a large number of process parameters, such as laser power, layer thickness, hatch distance and many more, must be adjusted. The complexity of the process results in unavoidable formation of process-related defects, such as porosities, incomplete fusion holes and cracks [47]. Since the increased occurrence of such defects affects the mechanical properties of the produced component, the reduction of those is crucial to ensure high component quality. Most of the research to date has focused on the optimization of process parameters. Therefore, the reduction of defects

takes place largely in the pre-process phase. However, the greatest advantages of SLM and AM in general, are the gained freedom in design and production. To allow greater freedom, defect reduction shifts towards the in-process phase, eventually allowing in-situ parameter adjustments and eliminating cost- and time-intensive pre-process research [11, 24].

2.1.1 Selective Laser Melting

SLM is a manufacturing technique building a component layer-by-layer by melting metal powder through high energy input provided by one or multiple lasers. The process is based on the SLS process, developed at the University of Texas at Austin in the mid-1980s for plastics [9] and further developed at Fraunhofer ILA for metals [25]. With the use of higher laser powers, with SLM it is possible to fully melt the metal powder, instead of only sintering. The main advantage of SLM over SLS is the significant reduction of post-processing. Current research focuses mainly on shorter construction times and larger volumes, the development of new materials and related parameters, and the monitoring of the process. The latter plays a major role in the research of still unsolved interrelationships as well as in the control of the process.
The process begins with the preparation of the CAD model using suitable pre-processing software to allow the upload to the SLM machine. Next, the build platform and -chamber is preheated to a set temperature, to prevent delamination of the initial layers.
The principle of SLM is depicted in Figure 2.1.1-1. In the next process step, a thin layer of

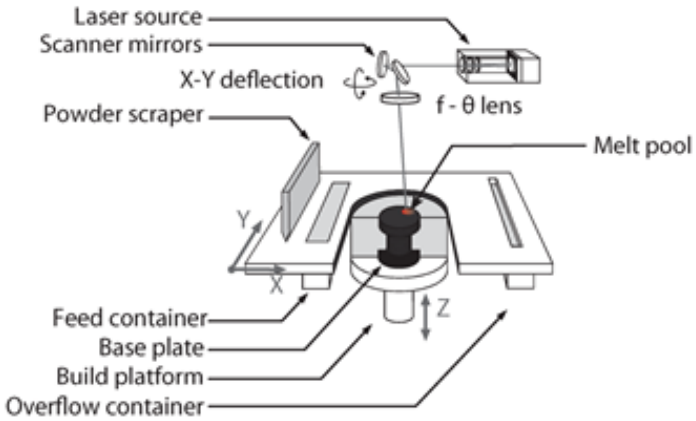

Figure 2.1.1-1: Schematic SLM process [7]

powder is paved onto the build platform with a powder scraper. Grain sizes vary depending on material and manufacturer between 10 μm and 60 μm, limiting the achievable layer thickness [1]. To avoid chemical reactions of the powder with the atmosphere inside the build chamber, it is flooded constantly with an inert gas, like argon. Through the scanner mirrors, a laser beam scans and melts the powder, following the uploaded scan paths, computed by the pre-processor. Due to the high energy input there is not only fusion of adjacent paths, but also between layers. This ensures cohesion of successive layers. Layer by layer, the components are built and finally cleaned and detached from the platform [48].

2.1.2 Defectreduction

The high freedom of design and ability to manufacture even highly complex structures in only one process step is achieved by utilizing a physical highly complex process, influenced by a multitude of parameters. In Figure 2.1.2-1 the most influential parameters, according to Aboulkhair et al. [2], are classified into four types: laser-related, scan-related, powder-related and temperature-related. According to Zhang et al. [47] the major factors related to

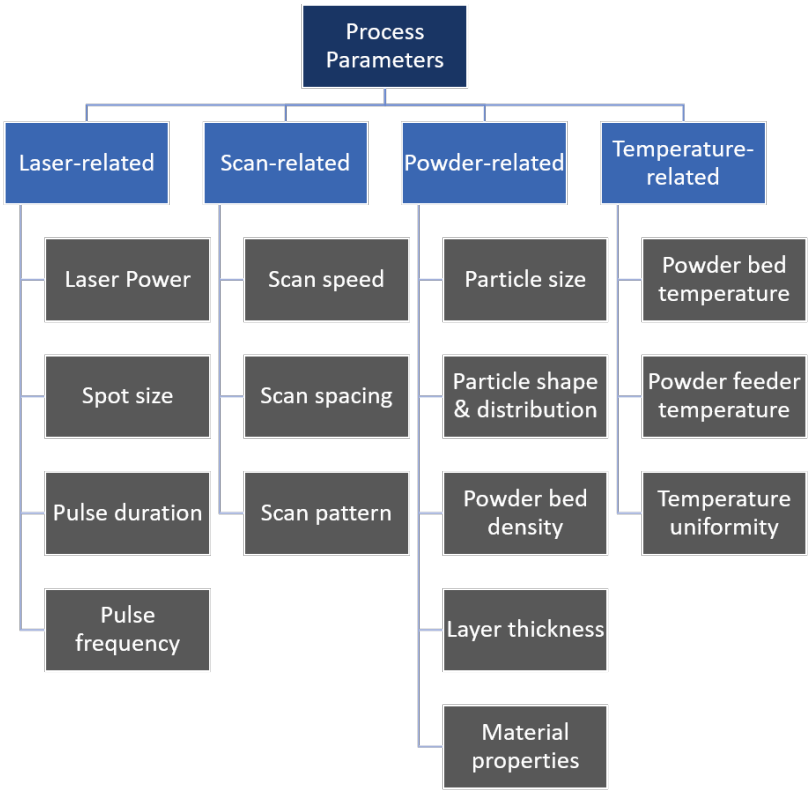

Figure 2.1.2-1: Most influential controlling parameters according to [2]

defect formation, that are set by the machine operator are energy input and scan strategy. In addition, the authors name the powder material as one of the most decisive influencing factors. The complexity of the process increases its susceptibility to defects and thus reduces the quality of the manufactured components.

Defects

As mentioned before, there are three major defect types: porosities, incomplete fusion holes and cracks.

Porosities are spherically shaped holes, with diameters typically less than 100 μm. These defects, also called keyhole pores, are entrapped gas bubbles in the melt pool as a result of high energy input or unstable process conditions [14, 29]. These defects are usually distributed evenly throughout the components and depending on the fabricated material are difficult or impossible to prevent.

However, incomplete fusion holes, or binding faults, usually originate in low energy input and with that a lack of fusion between successive layers. These kind of defects show a significantly

smaller sphericity than keyhole pores and are rather shaped like long narrow slits. The length of such defects however can be significantly larger up to multiple hundreds of micrometers [19].
According to Kasperovich et al. [19], the formation of these two defect types can be predicted by calculating the volume energy density E_V. The authors used TiAl6V4 and varied process parameters to investigate their correlation with the relative porosity of manufactured samples. With the major process parameters laser power P, scanning velocity v, hatch distance h and layer thickness t, the volume energy density can be calculated, see equation 2.1.2-1, which is a common integrated parameter to describe the energy input in the SLM process.

$$E_V = \frac{P}{v \times h \times t} \tag{2.1.2-1}$$

For lower volume energy densities ($E_V < 100\ \frac{J}{mm^3}$), the porosity increased due to formation of binding faults, as the lower energy input caused insufficient penetration of underlying layers. For energy densities above 130 $\frac{J}{mm^3}$ similarly an increase of the measured porosity was observed, caused by keyhole pores, whose amount grew with increasing energy density. An optimal volume energy density was found at $E_{opt} = 117\ \frac{J}{mm^3}$ [19].
The third defect type, cracks, occurs due to the locally rapid heating and cooling rates present in the melt pool. According to Gu et al. [16] the cooling rate of molten titanium reaches $10^8\ \frac{K}{s}$, resulting in large residual thermal stress in the component. This may cause cracks and delamination and with that even process- or component failure [16]. Other than the previously mentioned defects, with preheating and parameter optimization this defect can be eliminated entirely.

Reduction

To reduce the presented defects, in the past years parameter optimization has been the key method [6]. With further developments of integral parts of the machines, such as the laser source and mirroring systems as well as heated build platforms, the process control became more reliable. Controlling each parameter with higher accuracy and measuring potential defect causes, like the concentration of H_2, H_2O and O_2 in the supplied powder, increases stability of the process. In combination with numerical simulations, defects can be reduced prior to the process [28].
Additionally, defects can be reduced by size and number after the fabrication of the component. Hot isostatic pressing allows adjustments of the microstructure and even fusion of un-melted particles [47]. As Kasperovich et al [18] showed, this leads to improvements of the fatigue life of the built components.
The previously presented defect reduction methods require deep understanding of the process and supervision of the production by scientists or trained personnel. This discourages many companies from investing into AM. According to Everton et al [11] robust control of AM systems is a key challenge in order to increase adoption of AM. As the process is highly sensitive to changes in environmental and process variables, the primary task is to implement

closed-loop controls, enabling parameter changes in-situ without manual adjustment. The first step to achieve the goal of closed-loop AM is to monitor the process online.
Monitoring the build process can be achieved by placing a monitoring system in- or off-line. For in-line monitoring the reflected light is transmitted through the same lens and light path, as the laser beam on its way to the melt pool. A system developed by Berumen et al [4] with both a camera and photodiode is depicted in Figure 2.1.2-2. However, in-line systems

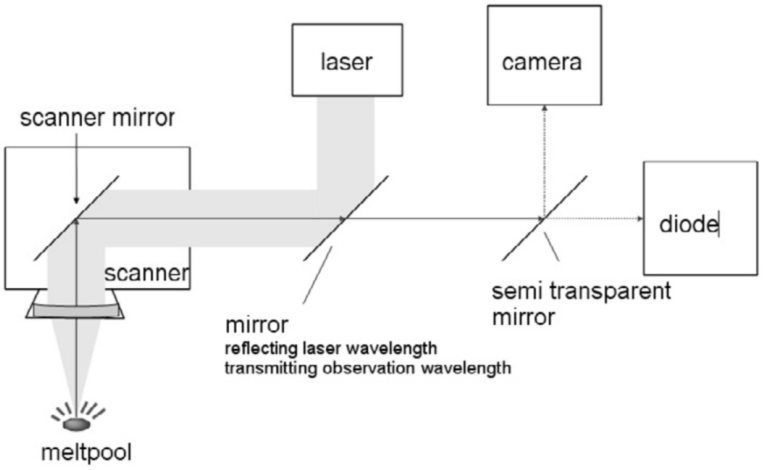

Figure 2.1.2-2: Schematic in-line process monitoring system [4]

limit the monitored area to the direct surroundings of the active build area. Systems relying solely on in-line photodiodes, like many commercial systems, do not provide thermal flow information.
Therefore, off-line monitoring systems are used to allow examination of the entire build. Using off-line high speed cameras in combination with in-line photodiodes provides both information of the current melt pool, as well as effects of the former to the entire powder bed. The use of multiple photodiodes with different sensitivities allows to split the reflected radiation into multiple measurements. As suggested by Yadav et al [45], the ratio of both intensities I_1 and I_2 correlates to the melt pool temperature. Even though computing the true temperature is not trivial, investigating the unitless intensity ratio provides useful information about the relative behavior of the melt pool.

2.2 Machine Learning

As a subset of Artificial Intelligence, ML gained more and more popularity in recent years, even though it has been a subject to research for many decades. Already in 1959 Samuel defined ML as a method for a computer to solve problems without being programmed to do so, but by learning from data instead [35]. Today, ML is used in a broad range of applications, among others: medical diagnostics, smart manufacturing, autonomous driving, natural language processing or finance [41]. Although ML consists of a constantly growing zoo of different approaches and algorithms, it can roughly be divided into three categories: supervised learning, unsupervised learning and reinforcement learning.

Supervised learning is often used in image processing and it requires a set of labeled data. The goal of such algorithms is to train a behavior with the labeled training dataset, so that an unlabeled testing dataset can be identified with the highest possible accuracy [41].
In contrast, unsupervised learning does not require labeled input data. This not only avoids data labeling, which can be a time-consuming task, but also allows predictions in data that is not known and therefore has the ability to uncover hidden interrelations in the data [42].
Reinforcement learning does not require a training phase or dataset, as the former do. Instead, the model learns by being punished or rewarded based on its trial and error behavior and by maximizing its reward. This paradigm has become very popular in the fields of robotics and autonomous driving as it allows steady improvement and to learn new behaviors by interaction with human operators [40].
Seeing is the sense to which humans are most sensitive. When driving, analyzing research data, interacting with one another, we rely heavily on our ability to process images in our brains. This might be the reason why computational vision is a method used in all kinds of fields of study. With that, image classification and object localization in images or videos still is a key challenge. Object detection combines the two tasks and outputs the input image with bounding boxes framing the detected objects in the image. This is often achieved by using supervised learning and neuronal networks. A key requirement in the context of process monitoring is the detection speed. Recently, very fast object detection algorithms have been developed, among others You Only Look Once (YOLO), achieving real-time predictions [32].

2.2.1 Neural Networks

(Artificial) Neural networks are mathematical constructions loosely based on biological neural networks. They consist of connected nodes, also called neurons. The neurons are arranged in different layers of the network, see Figure 2.2.1-1. Each network consists of one input layer, one output layer and a certain amount of hidden layers. For image classification, the input

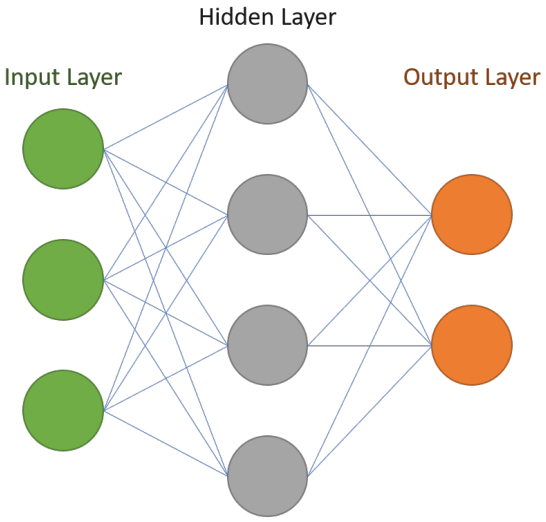

Figure 2.2.1-1: Schematic neural network with one input layer, one hidden layer and one output layer

layer usually consists of one (for grayscale images) or three (for RGB images) nodes per pixel. The output layer usually is a vector containing the probabilities for all classes. The nodes in the hidden layers are simply activation functions, for example sigmoid functions or ReLU functions. These activation functions generally compute the dot product of the connected nodes from the layer before and a vector of weights. The weights indicate how much the associated nodes affect the output of the function. This concept is derived from biological neurons, being activated if a certain input signal threshold is exceeded and sending the amplified signal to connected neurons. Usually, a network consists of multiple hidden layers which is why such kind of ML methods are called deep learning. In supervised learning, the prediction of the network is compared to the labeled data and the difference between the prediction, for example a vector of class probabilities, and the actual values shows how good or bad the network is performing. Typically the mean squared error is computed to output one single value indicating the performance. The function computing this performance index is called cost function. The goal of training is to minimize this cost function. The task to achieve this, is to change the weights in the hidden layers so that the output is closer to the desired values. This can be done by computing the gradient of the loss function with respect to each weight by applying the chain rule. Like so, the weights are updated after each iteration of training, until the cost function is as small as desired. The performance of the network at test time with images it has never seen before, is mostly depending on the diversity and amount of images fed to the network at training time. The more images showing the same object, but in a different angle or lighting the network has seen in training time, the more general the "understanding" of the network of this object will be [36].
Convolutional Neural Networks (CNN) are more suitable for object classification or detection in images. An image usually has three channels which results in a three dimensional input tensor. A convolutional layer in a CNN contains a number of n learnable filters whose size is usually much smaller than the image itself. The filters convolve, or slide, across the input image, computing dot products between the filter and the input. This results in a tensor of the width and height of the filter but with the depth of $3n$. Like so, the dimension is reduced until fitting the output tensor. This concept is especially applicable for image classification, as the use of filters for feature extraction has already been a common task in image processing. This leads to the network learning to recognize certain features occuring in images, increasing in complexity in layers further back [44].

2.2.2 Machine Learning in Additive Manufacturing

Wang et al [41] list eight use cases of ML related to AM, from design and topology optimization to process monitoring, manufacturing planning and data security they found in literature. They conclude however, that process monitoring is the major application of ML to date and is the subject of multiple publications.
Previous research on ML for AM process monitoring can be classified into acoustic-based and optical-based monitoring. Shevchik et al. [37] trained a CNN with acoustic signals emitted by plasma in the SLM process to classify porosity levels with a accuracy range between $83\ \% - 89\ \%$. However only three porosity levels where trained.

By far the majority of recent research in this field was done by processing optical data. Kwon et al. [21] applied a deep neural network to study classification of the melt pool in selective laser melting using labels for different laser powers. The data was gathered using an off-axial high speed camera. As described earlier, the porosity of a SLM manufactured component is linked to the energy input. Interchanging laser power, therefore produced different porosities which could be observed with the camera.
Also using deep neural network, Baumgartl et al. [3] used thermographic off-axis imaging to detect defects with an Infrared camera. Delamination and spatter defects were identified with a reported average accuracy of 96.8 %. CT scans were used to validate the results.
Gobert et al. [13] used images, taken by a DSLR and Computer Tomography (CT) scans and evaluated them using a linear Support Vector Machine. CT scans, taken of the produced parts were used to provide the ground truth for a binary classifier. For this, the images of the layers were segmented into neighborhoods. This allowed to detect defects such as overheating, pores and unmolten powder in-situ with accuracies greater than 80 %.
Using a thermal monitoring system and labeling with X-Ray images, Khanzadeh et al. [20] tested various supervised learning classification approaches like Decision Tree, K-Nearest Neighbor or Support Vector Machine.
Grasso et al. [15] used a high speed camera and k-means clustering in combination with Principal Component Analysis to automate defect detection. The camera was placed outside the build chamber and the goal was to detect local overheating phenomena. Although, due to variation in thermal flow, overhang structures could be detected, the approach is limited in its application, as data of successful builds of the exact geometry needs to be provided.
Finally Okaro et al. [26] implemented a semi-supervised classification algorithm by gathering heat radiation off-line with photodiodes. With tensile tests of the produced samples, the data was labeled according to the corresponding ultimate tensile strength of each sample.
In summary, the idea of automatic defect detection for in-situ process monitoring using ML has only recently been tested by a rather small group of researchers. Nonetheless, already a broad range of solutions has been presented.

3 Methodology

In this chapter the methods are presented, with which the data for this work were generated, processed and evaluated.
Figure 3-1 shows the individual tasks of the elaborated workflow. In the following, these

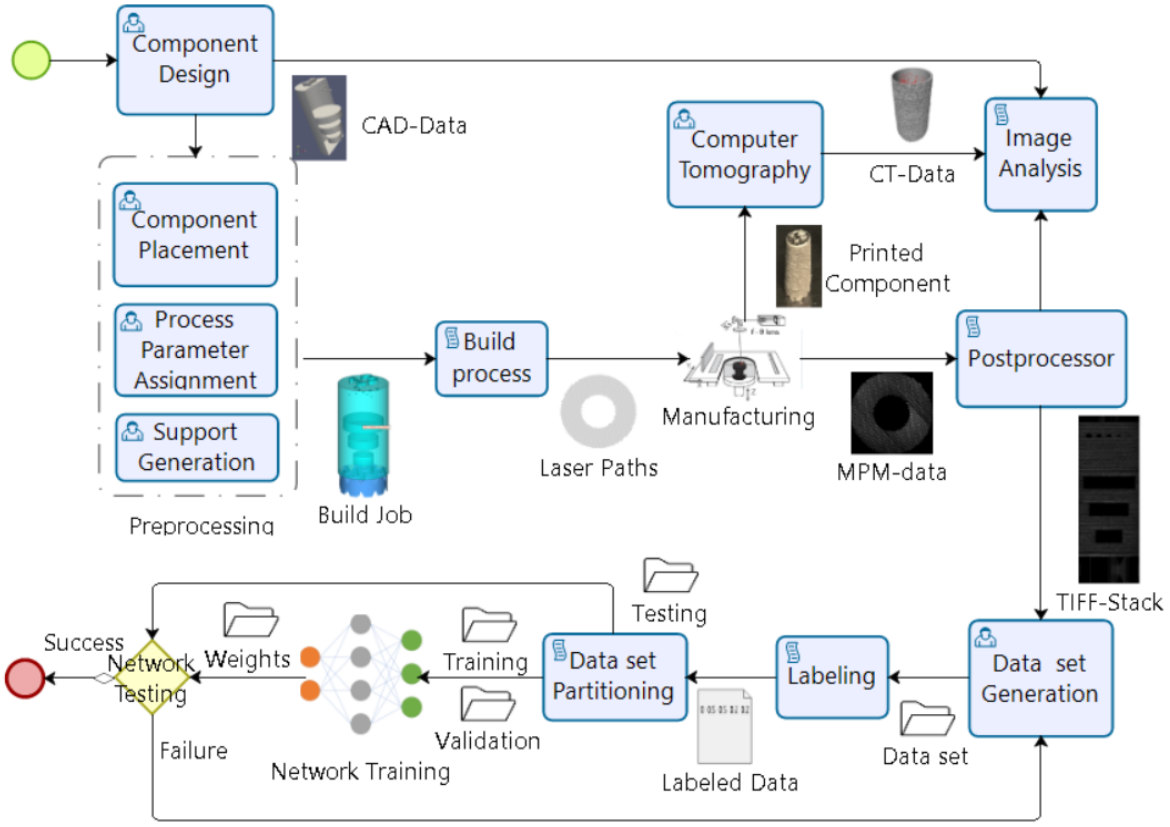

Figure 3-1: Elaborated workflow to train a CNN to detect defects in SLM components

tasks are described in detail. In order to successfully train a CNN, a large amount of data is necessary. Therefore, the first set of tasks are dedicated to Data Collection. For this, a set of samples is manufactured by Selective Laser Melting. Using the built-in Melt Pool Monitoring System (MPM), a large data set of raw Laser-Intensity data is gathered. The last task of Data Collection is the Post-processing which allows to export conventional image data, such as .tiff-stacks of each sample. After this first part the workflow splits into two main branches: a Deep Learning branch and an Image Analysis branch. For Image Analysis some general image information, like the mean gray values of each image, are computed. The computed data is visualized and compared to CAD- and CT-data. For Deep Learning on the other hand, data sets are generated and labeling of the objects to be detected is performed. A

selected, pre-trained CNN then trains these data sets. The last task in this workflow is the verification with test data.

3.1 Algorithm selection

As the selection of a ML algorithm dictates the post-processing of the gathered data, this should be done first.
The developed method should be as unrestricted and universally applicable as possible. In contrast to many previous research efforts, the entire workflow should be as easy to automate as possible and should also be usable for scientists and engineers from other disciplines after a short training period. This requires the fulfillment of some requirements, which are presented in the following.
In order to enable a universal and hardware-independent use in different scenarios, the use of external cameras should be avoided, unlike in most of the works cited. Instead, only the built-in pyrometry system consisting of two photodiodes is used. In order to allow the use of other camera systems, a method based on image data is chosen. This requires an intermediate step in the workflow to generate images from the collected data, but allows a universal and user-friendly application. It also allows the greatest possible wealth of experience to be utilized that has been accumulated in the field of image recognition in recent years.
A further requirement is the prediction speed with which the algorithm can process data. On the other hand, the goal is of course the highest possible accuracy. This is defined as the percentage of detected defects.
Furthermore, the used algorithm should already have been used in other, possibly even similar applications. This also results in the requirement for a simple implementation of the algorithm and easy integration into existing frameworks.
From the large number of algorithms and ML methods, the algorithm YOLO is particularly convincing due to its almost real-time capability with easy handling and convincing accuracy. In contrast to other object detection algorithms, YOLO is a single neural network that combines the two tasks of object localization and classification with just one ”look”, hence the name. The algorithm, developed by Redmon et al. [32], is particularly suitable for the application of in-situ defect detection, because many different types of defects can be trained step by step and the network, once implemented, can be easily adapted to new scenarios or image sources. The unique approach of YOLO shows good performance in generalizing the trained data. This means that it might be possible to train the network with data with a certain heritage, e.g. CT, and use data with a different heritage, e.g. MPM, in run-time. Furthermore, the algorithm convinces by its Darknet implementation. Darknet is an open source neural network framework that uses C and CUDAtechnology for performance reasons, but can also be used as PyTorch and TensorFlow implementation [31]. A disadvantage of this method of supervised learning is the rather time consuming creation of training data.

3.1.1 You Only Look Once

As mentioned, object detection, also referred to as object recognition, is the combination of two common ML tasks: image classification and object localization. In image classification, an image with a single object is processed by an algorithm and the aim is to name the object depicted somewhere in this image. Using a neural network of some sort, a dog classifier could be implemented by training the network with multiple images showing a dog. The output of this single class classifier is either "dog" or "no dog". The expected output of an image showing only one dog and of an image showing multiple dogs is equally "dog".
While for some cases classification alone is sufficient, most applications benefit through the prediction of number, size and position of objects in an image. The typical output of object detection are bounding boxes, framing the classified object. To achieve this, one approach, called sliding window, only classifies a portion or "window" of the whole image at a time. This "window" then "slides" over the entire image and each window is classified. If, for example, the image is 100 px by 100 px and a dog with a size of roughly 10 px by 10 px is located in the bottom right corner, the step size of the sliding window could be set to 50 px. This would mean, that the first image to be classified is the upper left 50 px by 50 px portion of the image. As no dog is present in this portion, it would be classified as "no dog". Next, the upper right, than the bottom left and finally the bottom right portions are classified. The last classification, of course classifies the portion as "dog". To detect the dog more precisely, the step size must be lowered, resulting in an increase of portions to be classified. For maximum precision with a step size of 1 px, the amount of portions is n^4 for an image of size $n\ px \times n\ px$, which results in a very compute intensive process [22], as for each portion the entire classification network needs to be run once.
While there are various optimizations of this and other methods increasing the speed, the approach of YOLO is different, as the object detection task is not separated into classification and localization. Instead, a single CNN is used by formulating a single regression problem for object detection. According to the authors the originally proposed implementation already runs at up to 150 fps [32] and more recent implementations of YOLO, such as YOLOv4 combine real-time speed with higher accuracy [5].
To achieve this, YOLO splits the input image into an adjustable amount of $S \times S$ grid cells. For each grid cell a set number of B bounding boxes, as well as a confidence value $P_r(Object)$ is predicted. $P_r(Object)$ represents how confident the network is, that this grid cell contains *any* object. The bounding boxes can extent far beyond their corresponding grid cell, but their center coordinates must lay within. To compute the accuracy of the prediction of a bounding box, intersection over union (IOU) between the predicted bounding box and the ground truth is used. The ground truth is the box, that is drawn in the labeling step and frames the object. The higher the overlap of the predicted box with the actual box, the higher IOU_{pred}^{truth}. To combine both predictions into one value, the confidence is computed by multiplying $P_r(Object)$ and IOU_{pred}^{truth}. Like so, $B * S * S$ predictions are computed, each consisting of 5 values: the position (x, y), the size (w, h) and the confidence. However, this is only the confidence for *any* object to be framed by the bounding box. To predict the class of the object, the conditional class probability $P_r(Class_i|Object)$ is predicted. *Conditional*,

meaning that $P_r(Class_i|Object)$ describes the probability that *if* the grid cell contains any object, that it than is an object of $Class_i$. Like so, each grid cell is classified, including those not showing any object. Equation 3.1.1-1 shows the final computation of the class-specific predictions by multiplication of the probabilities that there is an object, its size and that it is of $Class_i$.

$$P_r(Class_i|Object) * P_r(Object) * IOU_{pred}^{truth} \tag{3.1.1-1}$$

By thresholding, or non-max suppression, only predictions with high scores, meaning high confidence in class prediction and IOU, are considered [32].
The input of the CNN at test time is an image of any size that is than resized to 448 px by 448 px. The first layer of the network is therefore of size $448 \times 448 \times 3$, as each image has three channels: Red, Green, Blue (RGB). The output of the CNN is a tensor of size $S \times S \times (B * 5 + C)$, with C referring to the amount of classes predicted. For each of the B bounding boxes in each of the $S \times S$ cells x, y, w, h, the confidence and the class probability for each class is stored.
YOLO uses leaky rectified linear activation functions (leaky ReLU) for all convolutional layers, but the last that predicts class probabilities and bounding box coordinates, which uses a linear activation function instead [32]. A ReLU activation function is one that outputs the input value, if it is greater than 0, see equation 3.1.1-2.

$$f(x) = max(x, 0) \tag{3.1.1-2}$$

The evaluation of this function is very fast, but can lead to "dead" neurons. As gradient descent learning is applied, it is unlikely or even impossible for the neuron to recover when it is deactivated once, as its gradient is 0 for this case. To prevent this, leaky ReLU will not output zero, but a fraction of the input, see equation 3.1.1-3. However, the advantage of leaky ReLUs over regular ones in application is controversial [23].

$$f(x) = max(x, 0.1x) \tag{3.1.1-3}$$

Figure 3.1.1-1 shows the basic architecture of the original YOLO detection network with 24 convolutional layers.

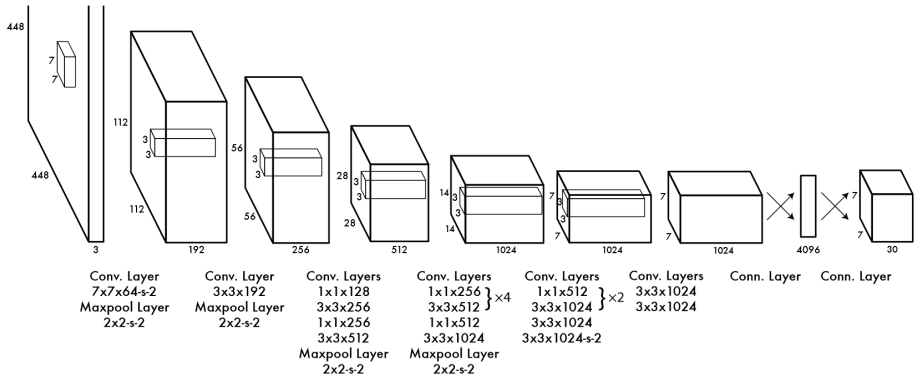

Figure 3.1.1-1: Original YOLO architecture [32].

3.1.2 YOLOv4 Implementation

YOLO has been developed and improved by Redmon et al. [32] until 2018 as an open source project. Bochkovskiy et al. [5] improved the source code to be more efficient for single GPU training and provided more data augmentation in training, which increases the accuracy without affecting the speed in test time. This implementation, as the original code by Redmon et al. is very easy to implement as it comes with the darknet framework. Another advantage of all available YOLO implementations is the rather straight-forward workflow to train the network with custom objects and the detailed documentation.

3.2 Data Collection

First, new data has to be generated by manufacturing various samples. For this a set of samples are designed and a build job is prepared. Then, the samples are manufactured and the collected data is processed.

3.2.1 Experiment Design

For this work a large set of 198 samples is manufactured and analyzed. To allow analysis by CT, many small instead of a few large samples are produced. CT allows to investigate the generated precision in production and presence of natural pores. In this work it is used mainly to detect the smallest possible cavity to be manufactured and compare the manufactured samples with the gathered data. Since the space for investigation for CT is limited, the basic design of each sample is a small cylinder with a diameter of 5 mm and a height of 10 mm.
Experimental experience in working with MPM-data at the Institute for Materials Research indicates that large artificial cavities in samples can be detected by analyzing the data of their cover layers. Due to the difference between the thermal conductivities of powder and molten metal, the intensities of the reflected radiation in layers directly above powder layers differs significantly from those in layers above previously molten material. To replicate this behavior, samples with artificial cavities of various sizes and shapes are manufactured.
As reported in chapter 2.1.1, common defect sizes in SLM Ti-6Al-4V range from a few μm up to a few hundred μm. However, the resolution of the SLM process is limited. In the direction of the scan vector the resolution of the process is only limited by the machine controller, stopping and starting the Laser source and can be neglected. In the direction perpendicular to the scan vector however, the resolution is limited by the hatch distance. Not taking other important parameters like the Laser beam diameter or scan velocity into account, the theoretical minimal diameter equals the chosen hatch distance of $h = 100\mu m$. In build direction, perpendicular to the build platform, the resolution is limited by the chosen layerthickness of $t = 30\mu m$. Considering both, common defect sizes and SLM resolution, cavities in the shape of spheres and cylinders with diameters ranging between 100 μm and 400 μm are expected to generate detectable and realistic data. The research conducted prior to this work however was carried out by investigating very large cylindrical cavities with diameters $d > 1000\ \mu m$. Thus, very large cylindrical cavities are designed also to verify previous findings and ensure

generation of usable data for further investigations.
Due to inhomogeneous build conditions throughout the build platform, each sample is produced with a redundancy of at least four, evenly distributed on the build platform. This ensures the independence of the results from the position of the samples. Furthermore, a larger amount of data is collected to increase precision of subsequent data analysis.
To further analyze the impact of Process Parameters and how this effects the Melt Pool, samples with three different process parameter sets are manufactured. Previous research by Kasperovich et al. [19] indicates that using certain parameter sets will provoke the formation of defects.

3.2.2 Sample Design

The samples are designed using the commercial software *Autodesk Inventor Professional 2020*. As mentioned, a 10 mm high cylinder with a diameter of 5 mm is used as a basic design for most manufactured samples. They vary in presence, shape and size of internal, artificial cavities. Five different designs are presented in the following: C-Series samples, featuring cylindrical cavities, S-Series samples, featuring spherical cavities, P-Series samples, featuring spherical cavities resulting in a certain porosity, N-Series samples without any artificial cavities and finally Parameter Stack samples.

C-Series

To verify the acquired experience, indicating large artificial cavities can be located by only analyzing MPM-data, a set of samples is designed with very large cylindrical cavities. Figure 3.2.2-1 shows the technical drawings of both samples. The two designs differ primarily in the height of the cylindrical cavities. The sample on the left, C_{1000}, has three big cavities with diameters of 2 mm, 3 mm and 4 mm and a height of 1 mm whose cylinder axes are aligned along the z-axis. The height of 1 mm is chosen, so that multiple layers of unmolten powder are provided. The distance between each cavity is 1 mm to prevent mutual interference. Above these cavities is a set of smaller cylindrical cavities whose cylinder axes are aligned either along the x-axis or the y-axis. These cavity designs are chosen to simulate cracks, that can form in different shapes, sizes and orientations. The cylinders aligned with the y-axis are 120 μm in depth with diameters ranging from 100 μm to 300 μm. Along the x-axis the cylinders with equal diameters have a depths of 180 μm.
The sample on the right, C_{2000}, is designed with two large cylindrical cavities, each 2 mm high with diameters of 2 mm and 4 mm. 9 mm off the ground, as in C_{1000}, there is a set of small, differently oriented cylindrical cavities. Again their diameters range between 100 μm and 300 μm and their depths are 500 μm and 560 μm.
However, the size of a typical pore ranges from a few to hundreds of μm, see chapter 2.1.2. Although samples with large cavities, as designed in C_{1000} and C_{2000}, are expected to show a noticeable effect, they are not representative for natural pores due to their size. Three samples are designed differing only in height of the inserted cavities. The first one, C_{30}, has cavities with a height of 30 μm, equaling only one layer. The second one, C_{60}, doubling the height to 60 μm, or two layers, and the third, C_{120} again doubling cavity height to 120 μm,

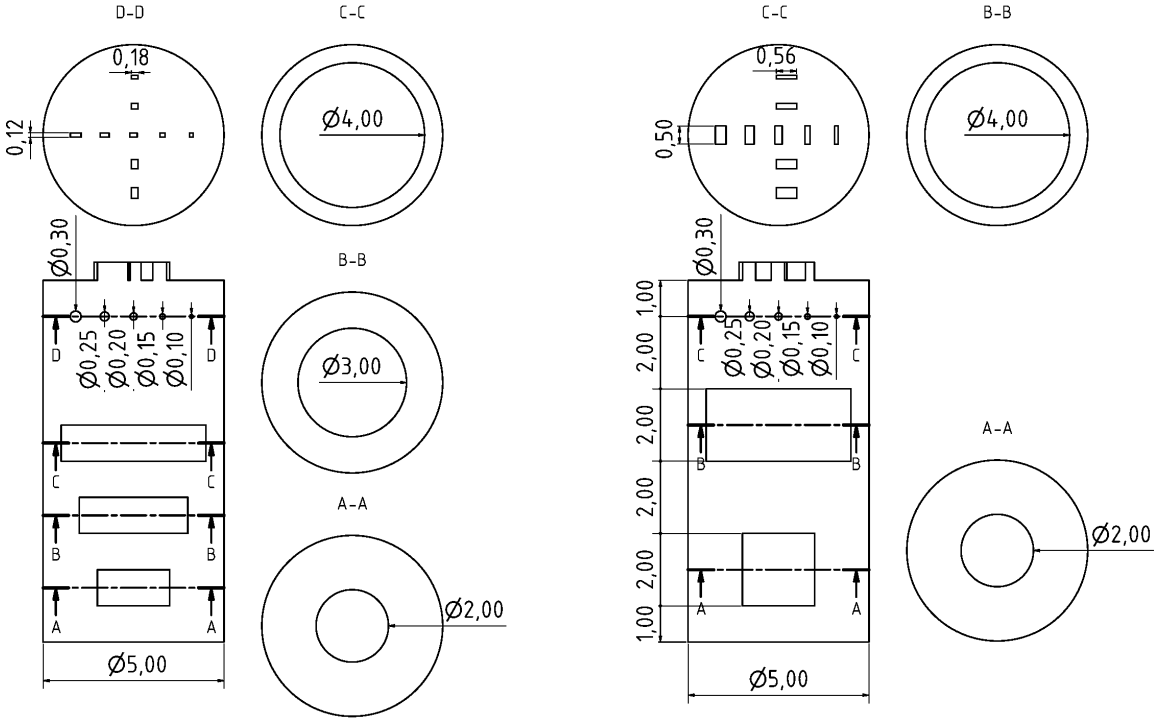

(a) Sample of type C_{1000} **(b)** Sample of type C_{2000}

Figure 3.2.2-1: Technical drawings of samples with large cylindrical cavities

equaling four layers of unmolten powder underneath the cover layer.
In all samples the placement of cavities is identical. Figure 3.2.2-2 shows the technical drawing and a sectional view of the sample C_{60}. The sample has a total of nine levels, separated by 1 mm. In each level three cavities are distributed evenly on a radius of 2 mm and again three on a radius of 1 mm, resulting in a spacing of 60 °. On each radius there is a cavity with a diameter of 100 μm, 200 μm and 300 μm. This design allows to observe a possible influence of the proximity to the sample center. In each level the arrangement of cavities is rotated by 30 °. This ensures the appearance of each cavity size in all possible positions and leads to rotational asymmetry which allows consideration of build direction in subsequent data-analysis. This way the positioning of the cavities can be interpreted as nine helices, screwing upwards from the bottom of the sample.

S-Series

To recreate the rather spherical keyhole pores observed by Kasperovich et al. [19] more accurately, a very similar design is chosen but with spherical cavities instead of cylindrical ones. Two samples are designed. One, called S_1, contains spherical cavities with diameters of 100 μm, 200 μm and 300 μm. The second, called S_2, has spherical cavities with diameters of 150 μm, 250 μm and 400 μm. Again, these cavities are positioned, as shown in Figure 3.2.2-3, in helices in the same manner as the samples of the C-Series.

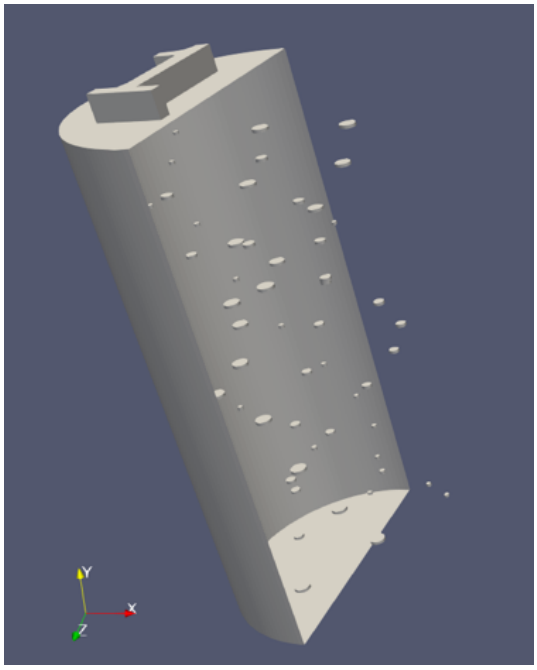

(a) Sectional view of a sample of type C_{60} with cylindrical cavities

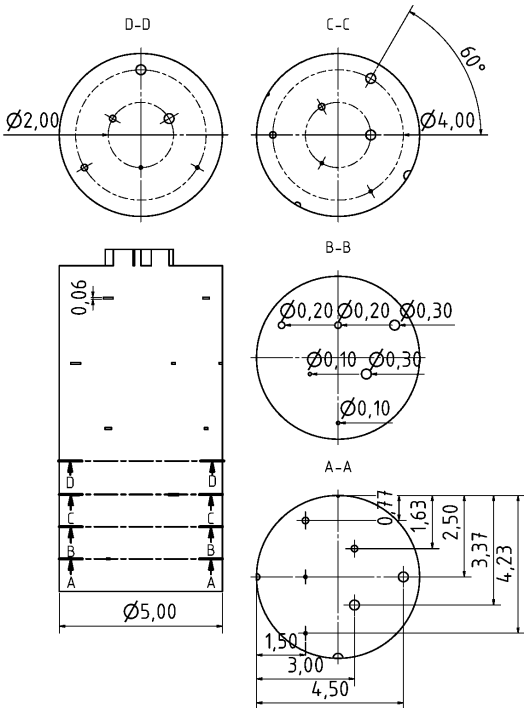

(b) Technical drawing of a sample of type C_{60} with cylindrical cavities

Figure 3.2.2-2: Design of the sample type C_{60}

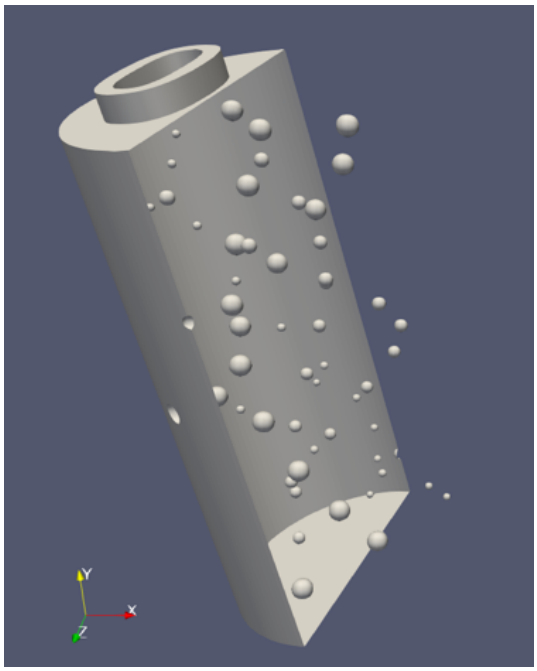

(a) Sectional view of a sample of type S_2 with spherical cavities

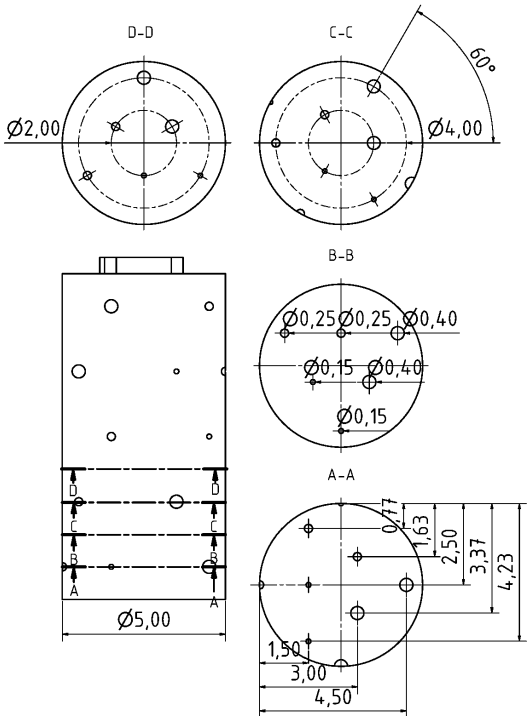

(b) Technical drawing of a sample of type S_2 with spherical cavities

Figure 3.2.2-3: Design of the sample type S_2

P-Series

The samples of this series are designed to not only provide more data of spherical cavities, but also allow to analyze how certain porosities in a layer affect the MPM-data in the layers above. For this, five more samples are designed. As before, the spherical cavities are positioned in nine levels along the z-axis, each 1 mm apart. In each level a 3 mm by 3 mm square is defined. This square is filled evenly with spherical cavities of varying sizes, so that the rounded share of cavity in each level is the same. Figure 3.2.2-4 shows an example of the distribution of cavities in the center plane. The in-plane porosity ϕ is calculated according to equation

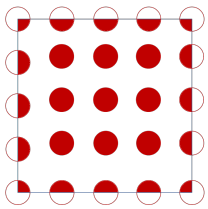

Figure 3.2.2-4: Schematic distribution of cavity center planes in a defined space. Parts of the cavities inside the space are filled.

3.2.2-1 from the number of circles within the square $N_{i,in}$, the radius of these circles r_i and the area of the square A_s. The parts of the circles that lie within the square are shown in red in figure 3.2.2-4. The number of circles inside the square $N_{i,in}$ is calculated according to equation 3.2.2-2, since 4 circles are inside the square at a quarter and $(a-2)$ circles at a half, where a indicates the number of circles on one edge of the square. Solving equation 3.2.2-1 for $N_{i,in}$, equating with equation 3.2.2-2 and resolving to a using the pq-formula results in a formula to calculate a, see equation 3.2.2-3. When applying the pq-formula only the case of addition is considered, because a number of cavities below 1 is not a valid result. Results are rounded to integers. Furthermore, this equation is only valid as long as the statement in equation 3.2.2-4 applies, which limits the ratio of porosity and maximal cavity size.

$$\phi = \frac{N_{i,in}\Pi r_i^2}{A_s} \tag{3.2.2-1}$$

$$N_{i,in} = a^2 - 2a + 1 \tag{3.2.2-2}$$

$$a = 1 + \sqrt{\frac{\phi A_s}{\Pi r_i^2} - \frac{3}{4}} \tag{3.2.2-3}$$

$$\frac{\phi}{r_i^2} > \frac{3\Pi}{4} A_s \tag{3.2.2-4}$$

For the first sample, P1, in each level a share of 1% is aimed for. The cavities in the lowest level are 30 μm in diameter, resulting in a total number of $12^2 = 144$ cavities. With each of the nine levels the diameters of corresponding cavities grow by 30 μm. Resulting in cavities 270 μm in diameter, and a total of amount of only $2^2 = 4$ cavities in the uppermost level. The samples P_2, P_3 and P_5 are designed similarly but with rounded shares of 2%, 3% and 5% of cavities in each of the nine levels. The last sample in this series, P_{Var}, is designed not with a fixed share of cavities in each level, but with a fixed spacing across all levels. The radii of the cavities increase from by layer along the z-axis, as for the other samples of this

series. Thus, the share of cavities increases from bottom to top. Figure 3.2.2-5 shows the technical drawing and sectional view of P_1. Technical drawings of all samples can be found in Appendix A.

N-Series

Several samples are manufactured without any artificial cavities. By assigning different process parameters, the findings of Kasperovich et al. [19] can be verified and their possible impact in the gathered MPM-data can be investigated. Again, to ensure the samples can be analyzed using CT all samples are designed as cylinders, 5 mm in diameter and 10 mm high.

Parameter Stacks

Additionally, four larger samples without artificial cavities are manufactured. These Parameter Stacks are designed by stacking five, 2 mm high cylinders with a diameter of 5 mm, on top of each other. This design allows to assign each cylinder one individual process parameter set.

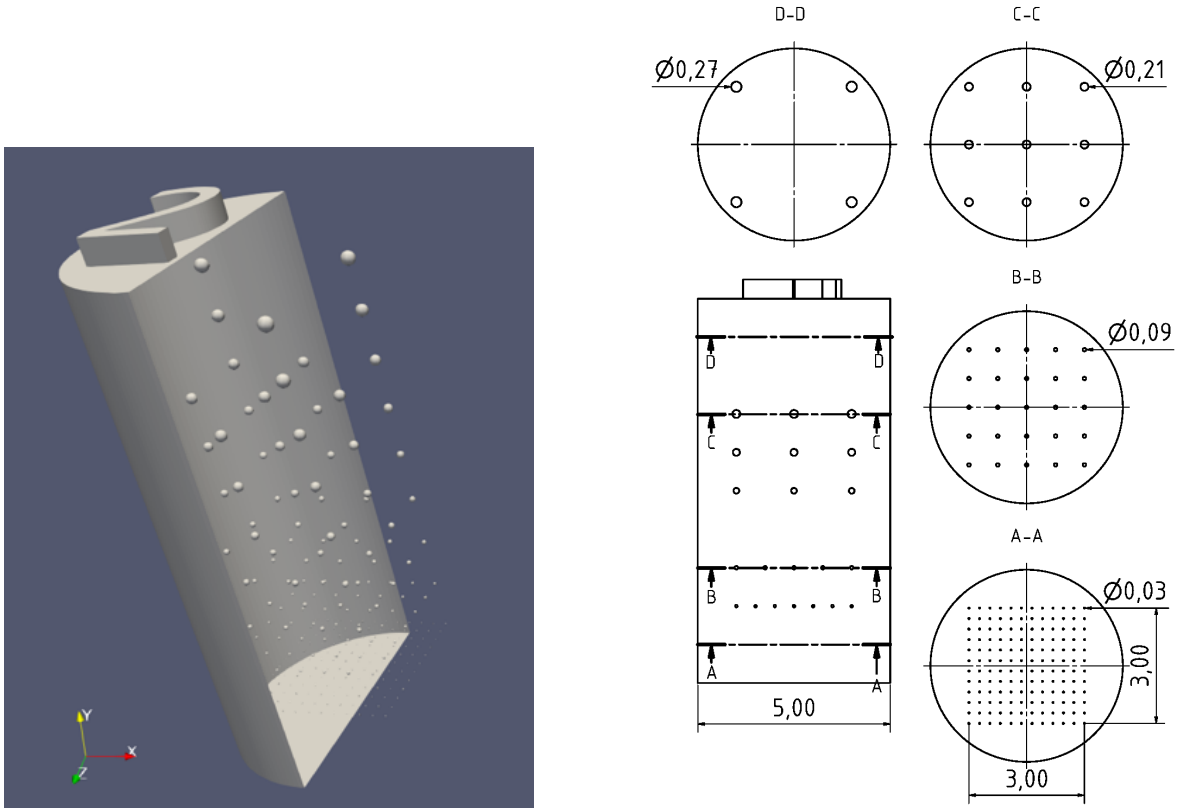

(a) Sectional view of a sample of type P_1.

(b) Technical drawing of a sample of type P_1

Figure 3.2.2-5: Design of the sample type P_1 with spherical cavities and in-plane porosity of 1 %

3.2.3 Build Preparation

The next task in Data Collection is to prepare the build job. For data and build preparation the commercial software *Materialise Magics* is used. Before the samples can be manufactured,

various steps of preparation must be completed. These steps include Positioning, Support Generation, Process Parameter Assignment and Slicing.

Positioning

As mentioned before, each sample is placed in multiple locations on the build platform to reduce positional effects as well as increase redundancy. Figure 3.2.3-1 shows the top view of the build platform. The different sample types are distinguished by color and shape. All samples with cylindrical cavities ($C_{1000}, C_{2000}, C_{30}, C_{60}, C_{120}$) are colored in red. Samples S_1 and S_2 are colored in blue. Samples with certain percentages of defects ($P_1, P_2, P_3, P_5, P_{Var}$) are represented green. Samples with natural pores (N_1, N_2, N_3) are colored in gray. Finally, the Parameter Stack samples are colored in brown.
The build platform is separated into nine segments, which are named as a combination of their row (Top, Middle, Bottom) and column (Left, Middle, Right): TopLeft (TL), TopMiddle (TM), etc. In each of the five segments TL, TR, MM, BL, BR there is one sample of the previously mentioned ones with artificial cavities. Adding to those twelve samples are six samples with natural pores, two of each type.
A copy of each sample with artificial pores is positioned 12 mm above the build platform. Due to the smaller number of samples in this height, the effect of shorter build times can be analyzed. This results in 30 samples in each of the five segments or 150 in total. Adding to those, in each of the four segments TM, ML, MR, BM there is one more sample of each type with artificial pores, resulting in additional 48 samples. Also, four Parameter Stack samples are positioned on the build platform. In total 198 samples are positioned on the build platform. To prevent interference from thermal radiation the samples are positioned with a minimum distance of 5 mm. The design of the P-Series samples was not tested prior to this work and is suspected to be potentially error-prone when being manufactured. Therefore, the samples are positioned with greater distance to other samples to avoid destruction of adjacent samples. To further lower the risk of an error in one sample destroying adjacent samples, the samples are positioned out of line. This way, if the powder bed is disturbed due to an error in one sample, consequential damage can be reduced.
The build time of one layer is limited downwards by 60 s, which allows for the laser and power bed to cool before the next layer is exposed. To homogenize the cooling time, a total of three empty samples are manufactured with a power of 0 W, located to the left, to the right and above the middle section. This will lead to three short breaks during the build of each layer.

Support Generation

To ensure samples are not manufactured directly onto the build platform, a 2 mm high support is generated. This support structure needs to allow easy mechanical removal of the samples with hammer and chisel. Therefore, the contact area between support and build platform as well as the sample needs to me minimized. This also minimizes the build time. At the same time, a solid connection is essential to prevent build crashes due to delamination and to ensure an even surface for the part to be built upon. Another key feature of the

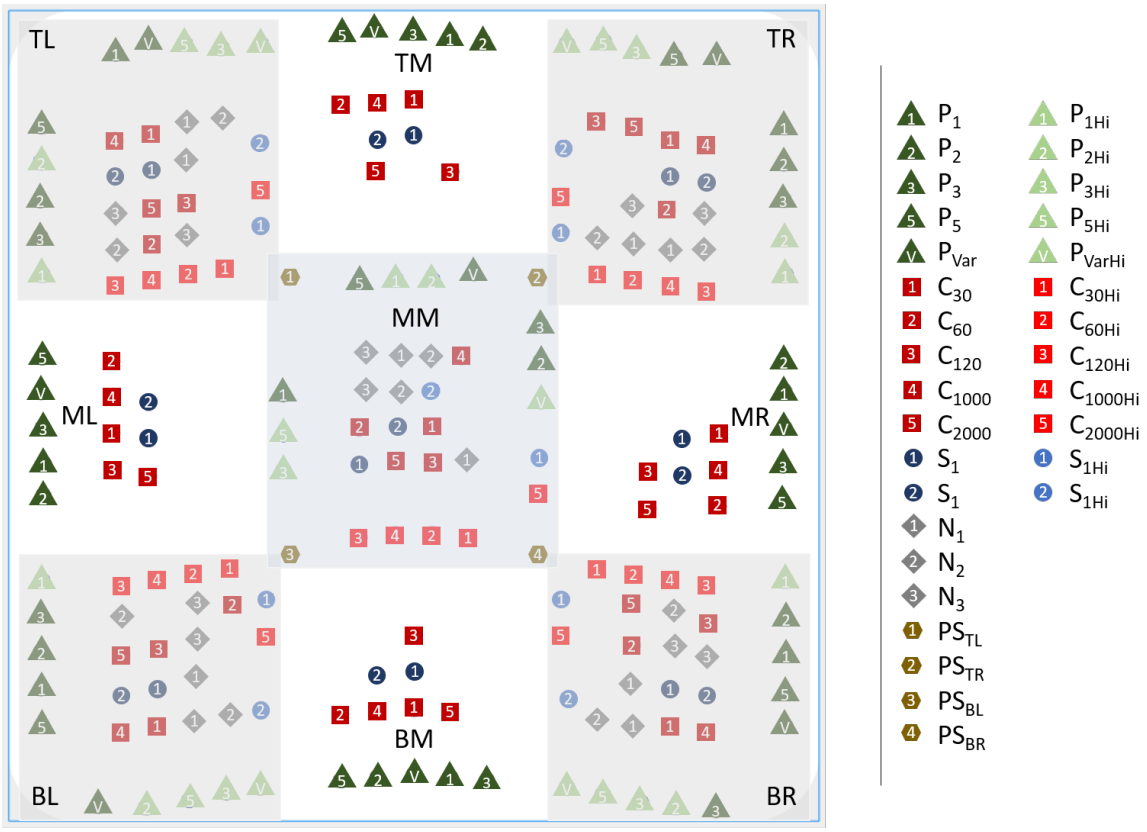

Figure 3.2.3-1: Sample positioning on the build platform. Blue circles: S-Series, red squares: C-Series, green triangles: P-Series, gray diamonds: N-Series, brown hexagons: Parameter Stacks, in lighter colors the samples with 12 *mm* support.

support structure is to increase thermal homogeneity throughout the build volume prior to part manufacturing. The chosen support structure depicted in Figure 3.2.3-2a meets these requirements.

Figure 3.2.3-2b shows the top layer of the support structure onto which the first layer of the part is manufactured. In order to assure the structural integrity of the part manufactured on top, a thin wall is generated along the circumference which is continuous in the middle and tapers in peaks both towards the build platform and towards the component above so that the contact area is minimized simultaneously. The inner of the structure is designed in a similar fashion with thin, tapered walls with a checkered layout. The support structure extends over 5 layers into the workpiece produced above to guarantee a structurally strong connection.

Using automatic support generation provided by the used software *Materialise Magics*, cavities are filled with support structures to ensure structural integrity of the cover layers. These supports are deleted manually, as the goal is the analysis of cover layers with empty cavities underneath.

Process Parameter Assignment

As mentioned in chapter 2.1.2 Kasperovich et al. found a porosity-optimized process window for SLM Ti-6Al-4V. Three parameter sets compared in their work are used. They are

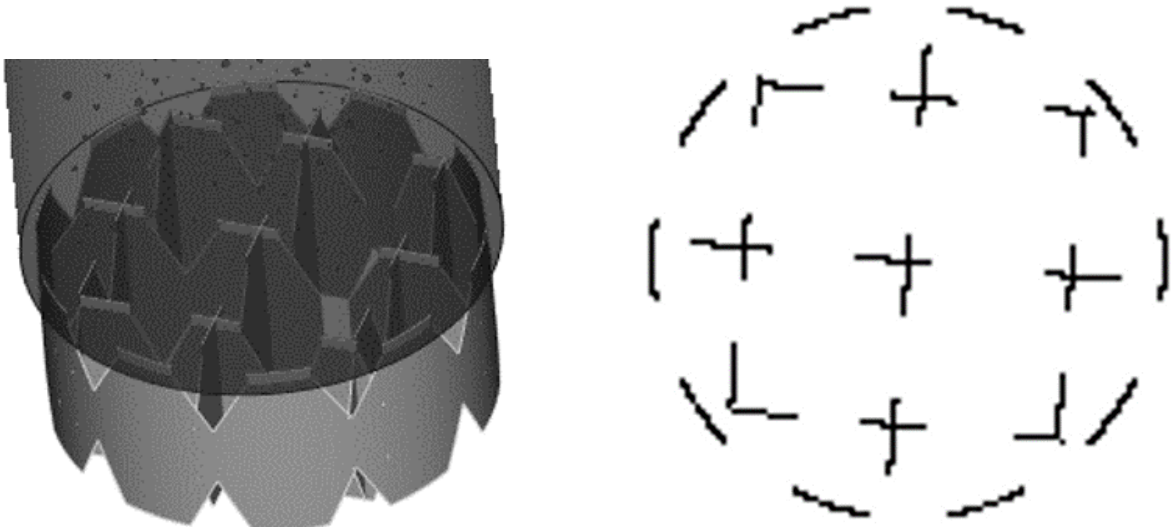

(a) Generated support structure underneath a sample

(b) Uppermost layer of the support structure onto which the sample is manufactured

Figure 3.2.3-2: Support structure

called A1, A4 and A9, referring to their volume energy density: $E_V^{A1} = 58\ \frac{J}{mm^3}, E_V^{A4} = 117\ \frac{J}{mm^3}, E_V^{A9} = 292\ \frac{J}{mm^3}$

All samples with artificial cavities (C-Series, S-Series, P-Series) are manufactured with the porosity-optimized parameter A4, so that effects due to natural defects are minimized. To ensure cover layers above cavities to be manufactured as if the cavity would not exist, options for special treatments of such layers, which are used in default parameter sets, are deselected. The samples with artificial cavities in the segments TL, TR, MM, BL, BR are manufactured without edge contours, whereas the samples in segments TM, ML, MR, BM are manufactured with edge contours. This includes edge contours around cavities, as well as the edge contour of the samples itself. While production without edge contours is expected to generate data more similar to natural defects, it is also expected that edge contours help to preserve the shape of the cavities. Manufacturing identical samples with both options allows to analyze its effect in future research.

Samples N_1 are manufactured with process parameters A1, samples N_2 with parameters A4 and samples N_3 with parameters A9. All of these samples are manufactured without edge contours. This allows analysis of the surface in further research and prevents effects of these contours to show in the gathered data.

Slicing

After the sample design, positioning and parameter assignment, the last step of data preparation is slicing. In this step a machine dependent processor is used to calculate laser paths. For the whole build job a unified scan strategy is used. All filling contours are manufactured with a cross-hatching scan strategy with zigzag scan vectors. In Figure 3.2.3-3 the calculated paths of a C_{60} sample manufactured with edge contours are shown on the left. The present edge contour is depicted in red. All edge contours consist of two paths. On the right Figure 3.2.3-3 shows the paths of the same sample manufactured without edge contours. The scan

pattern is projected onto to the entire build platform by the build processor. This causes changes of direction of the scan vectors, as visible in the top left of the layer without edge contours on the right. In chapter 4.3.2 a possible effect of this scan strategy is discussed.

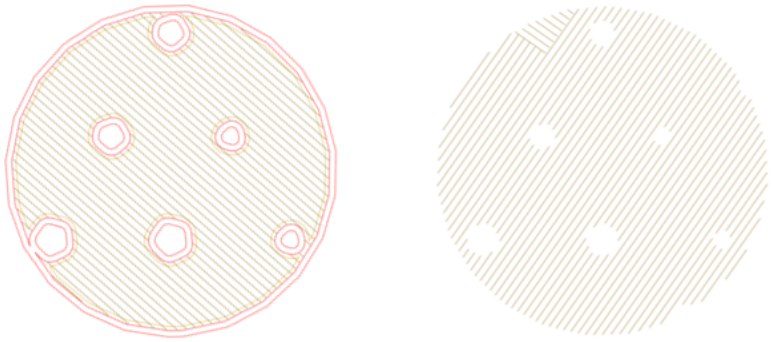

Figure 3.2.3-3: Computed laser paths of the same layer of two C_{60} samples, one with (left) and the other without (right) edge contours

3.2.4 Manufacturing

The computed paths are then uploaded directly to the controller of a SLM machine. The prepared build job is executed using a SLM 250HL Laser Beam Melting System by SLM Solutions GmbH. The machine is equipped with a 400 W YLR-fiber-laser and offers a 350 mm high build chamber with a 248 mm by 248 mm heated build platform. The layer thickness can be adjusted between 20 μm and 100 μm, the scan line can be adjusted downwards up to 150 μm. The samples for this work are produced in an argon atmosphere that was preheated to 200 $°C$. This temperature is held constant throughout the build job. The concentration of oxygen and hydrogen are measured constantly, and inflowing gas is purified. The reused Ti-Al6-V4 powder is provided by SLM Solutions and is prepared by sieving in a glove box, which has negligible effect on build quality, according to Quintana et al. [30]. The MPM-System by SLM Solutions GmbH is set to measure with its highest possible frequency of 100kHz. As described in greater detail in chapter 2.1.2, during manufacturing the reflected radiation of the Laser is collected in-line with two diodes and saved with the associated position data. This MPM-data can be exported from the machine for further processing and investigation.

3.3 Deep Learning MPM Images

After the samples or components are manufactured and the MPM-data is gathered, it needs to be processed to fit the input requirements of YOLO. For this, first the raw MPM-data is processed using a designated software. Then, the processed data needs to be divided into data sets, so that only the data needed can be filtered. Furthermore, a ground truth must be generated, which is also called labeling. Finally, the CNN is trained and its performance needs to be evaluated.

3.3.1 Data Processing

Using the *MPM-Viewer* software, developed at the Institute for Software Technology, the machine data can be read and visualized. Also, this software is used to export the data to images with which the CNN can be trained.
The software allows to select between three channels: Intensity 1, Intensity 2 and the quotient of Intensity 2 and Intensity 1. The channels Intensity 1 and Intensity 2 vary in wavelength. For this work the quotient of both was used, as it is expected to best represent the temperature of the melt pool. The software also allows to adjust the colormap and set upper and lower limits. Although a colormap ranging from blue (lower values) to red (higher values) is most common, as it is comfortable for the human eye, in this work mostly grayscale images are used, as it simplifies data analysis. To enable qualitative comparison of the data, equal limits for color mapping are applied to all processed data.
Using the provided "Region Selection" Tool, individual samples are selected for analysis in the Viewer and exported as .tiff-stacks. This allows to build a database with all layers of all samples to be analyzed.
Moreover, the displayed data resolution can be adjusted in all three dimensions. Figure 3.3.1-1 shows three representations of the same data with three different resolutions. The data on the left in Figure 3.3.1-1a is exported with a resolution of 100 μm along both the x- and y-axis. Although the hatch distance is also 100 μm, individual laser tracks cannot be distinguished from one another, as they do not align with one of both axis. With that, the brightness of each pixel is computed by linear interpolation, which leads to a decrease of accuracy. Edges are visualized very rough and small objects, like the cavities in the upper right of the sample can hardly be detected by eye. Although lacking accuracy, this representation results in images with sizes of only 50 px by 50 px, which is useful as a large amount of images has to processed in various steps, so file size is a critical parameter.
On the right hand side in Figure 3.3.1-1c the same data is visualized with the highest possible resolution of 4.8 μm. Like this, not only individual laser tracks can be distinguished, no matter their direction, but even individual data points are visualized. With a measuring frequency of 100 kHz of the MPM-System and a scan vector speed of 525 $\frac{mm}{s}$ the distance between adjacent data points is at 5.25 μm just above the resolution of 4.8 μm. This representation offers a maximum of accuracy and precision, as virtually no interpolation is performed and no data is lost. However, the image of one layer in one sample has a size of 1115 px by 1115 px, resulting in very large file-sizes of multiple Megabyte per image, depending on the actual data. Moreover, the huge difference between the width of a pixel of 4.8 μm and the hatch distance of 100 μm leads to very large empty parts in the image. As a Deep Learning framework is used, that is engineered with photographs of real objects in mind, it is expected that objects to be detected should be as visible to the human eye, as good as possible.
Therefore, a resolution of 50 μm is chosen, resulting in images like the one in the middle in Figure 3.3.1-1b. This resolution is small enough, so that empty space between laser tracks is minimized, while the accuracy is high enough to depict even small cavities. Images have a reasonable size of 100 px by 100 px to allow fast and smooth processing. Visualized data points are computed by averaging.

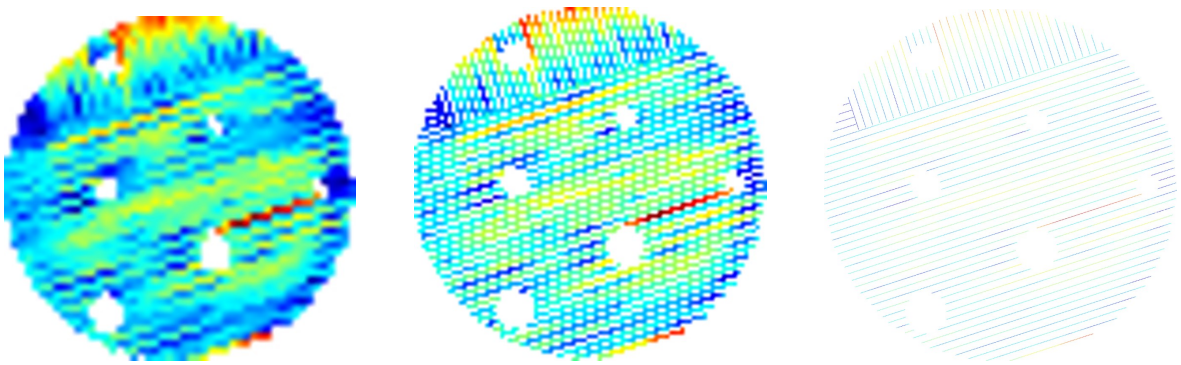

(a) With a resolution of 100 μm **(b)** With a resolution of 50 μm **(c)** With a resolution of 4.8 μm

Figure 3.3.1-1: MPM-data of a sample of type C_{60} in three different resolutions.

3.3.2 Data Set Composition

A total of five data sets is created from the collected data. Four of these data sets contain certain layers of selected samples. The fifth set consists of images containing the whole build job.
The stack position i of an image can be calculated with

$$i = \frac{z + h_{support}}{t}, \tag{3.3.2-1}$$

where $h_{support}$ is the height of the support and t is the layer thickness. Like this, z-Positions z from the technical drawings, shown above, can be converted to select chosen layers from the sample data sets.

3.3.3 Creating Ground Truth

Since YOLOv4, a supervised learning algorithm, is used, a ground truth must be created. This is done by labeling all objects in the dataset. In darknet format, two file types are essential for labeling. Each dataset must have one *labels-file*, a labelmap, in which all class names are listed, one in each line. For the most part of this work there is only one class to be detected which is called “cavity”. Furthermore, a simple .txt-file with the same name as the corresponding image is required, storing the class ID, position and size of the object.
Labeling can be done manually with dedicated software, like LabelImg. However, the presented data sets consist of only a limit amount of different images. Therefore, labeling is done by using information from the sample designs and labeling images batch-wise by following the workflow depicted in Figure 3.3.3-1. In the first step, a labelmap is created. For this, a text-file is generated containing all class-names, used in the data set.
Then, the data set is subdivided into multiple subsets, each subset only containing images with cavities located at the same position and equal in size. For each subset the position and size of all present cavities is taken from the design of the corresponding sample. To meet format-specifications, x-values are measured from the left and y-values are measured from the top of the sample.

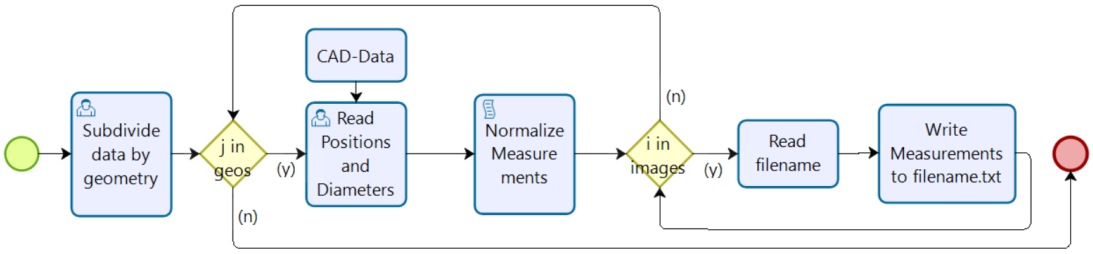

Figure 3.3.3-1: Workflow of the semi-automatic labeling process

The next step is to normalize these values. This is done by dividing the measurements by the width of the image, which corresponds to the diameter of the sample $d = 5\ mm$, see equation 3.3.3-3.

$$x_{norm} = \frac{x_c}{d} \tag{3.3.3-1}$$

$$y_{norm} = \frac{y_c}{d} \tag{3.3.3-2}$$

$$w_{norm} = h_{norm} = \frac{d_c}{d} \tag{3.3.3-3}$$

This normalization to range $[0, 1]$ is done to simplify the application of data augmentation like scaling or stretching performed by the darknet framework.
Subsequently, a text-file is created and class ID, x_{norm}, y_{norm}, w_{norm} and h_{norm} are written in one line, separated by whitespaces and it is named identical to the current image. This is repeated for all cavities in this image and for all images in the current subset, as positions and sizes of objects are equal.
Iterating through all subsets, providing the corresponding measurements from the design, the whole data set is labeled. Figure 3.3.3-2 shows the input and output data of an example image. The bounding boxes, colored in red, framing the cavities, are only depicted for presentation purposes.

3.3.4 Training

In the next step, the data set, now consisting of image files and corresponding text files, is divided into three: training, validation and testing. For this, first all data is moved from subsets to one folder. About $10-20\%$ of the data set should be reserved for validation, another 10 % for testing and the remaining images are used for training. For this task a simple script is written to randomly move the necessary quantity of images into the designated folder. Picking data randomly ensures a uniform distribution for larger data sets. Furthermore, the amount of labeled images is matched by the same amount of images without objects of any class present. However, an empty .txt-file must be provided. This is done to prevent the assumption that every image has at least one object present.
The last step prior to training the network is to adjust the configuration-file of the YOLOv4 implementation. In this file the architecture of the neural network is stored. Here, the number of classes to be trained is adjusted and the number of iterations is selected.

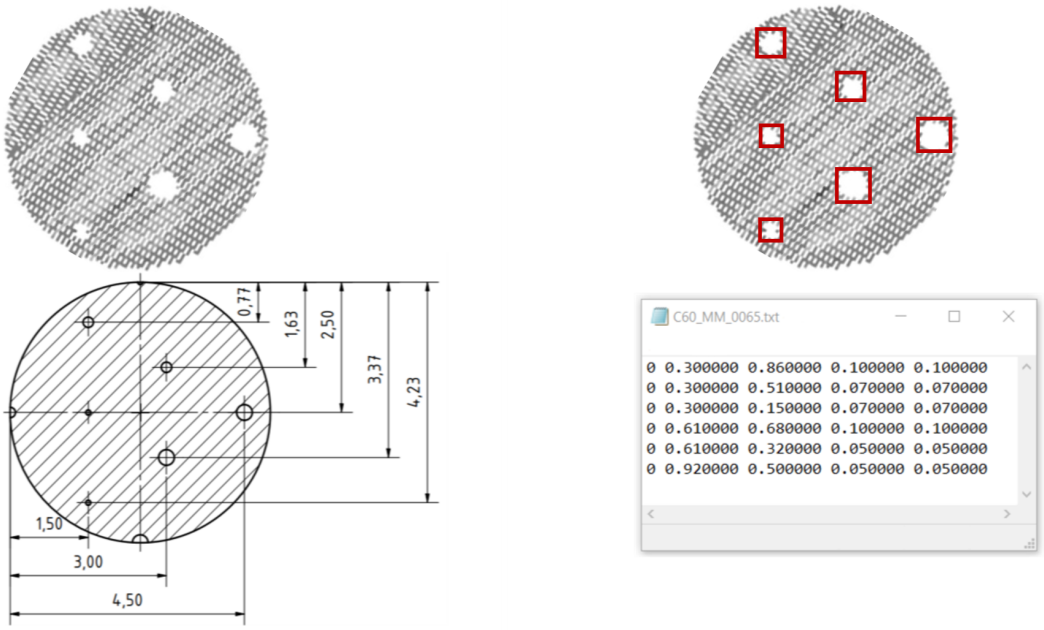

(a) Input: image, measurements **(b)** Output: .txt label-file in darknet format

Figure 3.3.3-2: Input data and output data of the labeling workflow

For this work darknet is built using Google Colab, a cloud collaboration tool providing GPU usage. Training is carried out on a Tesla T4 GPU by NVidia. Prior to training with each data set, the network is updated with weights provided by the developers of YOLOv4, Bochkovskiy et al. [5].

3.3.5 Evaluation

For evaluation purposes, the mean average precision (mAP) and Average loss are recorded during training. Everingham et al., the authors of "The PASCAL Visual Object Classes (VOC) Challenge" [10], define mAP by evaluating the precision/recall curve.
Precision is a measure calculated by diving the amount of true positive predictions by the amount all positive predictions, including false positives, giving the percentage of correct predictions. Recall is measured by dividing the amount of true positives by the amount of actual positives, or the sum of true positives and false negatives. The mAP is calculated by interpolating and averaging eleven data points on the precision/recall curve [10].
Average loss refers to the output of the cost function, also called loss function. The loss function of YOLO is shown in equation 3.3.5-1 and consists of multiple parts. The first part penalizes positional error and the second part the error in size of the bounding box. The third and fourth part of the equation represent the error of classification of any object and

the last part penalizes the error in class prediction. This loss function is optimized during network training.

$$\begin{aligned}
&\lambda_{coord} \sum_{i=0}^{S^2} \sum_{j=0}^{B} 1_{ij}^{obj} [(x_i - \hat{x_i})^2 + (y_i - \hat{y_i})^2] \\
&+ \lambda_{coord} \sum_{i=0}^{S^2} \sum_{j=0}^{B} 1_{ij}^{obj} [(\sqrt{w_i} - \sqrt{\hat{x_i}})^2 + (\sqrt{y_i}) - \sqrt{\hat{y_i}})^2] \\
&+ \sum_{i=0}^{S^2} \sum_{j=0}^{B} 1_{ij}^{obj} (C_i - \hat{C_i})^2 \\
&+ \lambda_{noobj} \sum_{i=0}^{S^2} \sum_{j=0}^{B} 1_{ij}^{noobj} (C_i - \hat{C_i})^2 \\
&+ \sum_{i=0}^{S^2} 1_{ij}^{obj} \sum_{c \in classes} (p_i(c) - \hat{p_i}(c))^2
\end{aligned} \tag{3.3.5-1}$$

3.4 Data Analysis

The aim of this analysis is to asses the quality of the collected data and to help evaluate the results of the preceded Deep Learning workflow. To analyze the exported .tiff-stacks, the software *ImageJ* [34] is used. The chosen grayscale color mapping allows to convert the RGB .tiff-files to 8 *bit* grayscale .tiff-files for data analysis without loss of information. The 8 *bit* grayscale data sets are analyzed by measuring the mean gray value of each image in an image stack.

For analysis, the following samples are investigated: C_{1000}, C_{2000}, C_{60}, S_2, P_5, P_{Var}, N_1, N_2, N_3 and all four Parameter Stacks.

To compare the measured MPM-data with CAD-data and the actual manufactured sample, CT is performed for samples P_5 and P_{Var}. These samples are chosen, as it is expected they will not only provide data to be compared to MPM-data, but also allow the resolution limit of the SLM process to be investigated. Using the 3D-Viewer plugin for *ImageJ*, sectional views are created and correlated with sectional views of the sample designs.

4 Results and Discussion

In this chapter the results achieved with the developed workflow are presented and discussed. Using the code and methods described in chapter 3, multiple data sets are composed and the data is analyzed both conventionally and by training the presented CNN YOLOv4. First, large cavities, as detected in previous research, are analyzed and the results of image analysis and the CNN are compared. Then the workflow is used to detect smaller cavities in the data. Finally, the influence of chosen parameter sets and further influences are analyzed and discussed and the elaborated workflow is evaluated.

4.1 Data set *Big Cavities*

The first composed data set *Big Cavities* consists only of the samples of type C_{1000} and C_{2000}. Before the data set is used for Deep Learning, it is analyzed by computing mean-intensity values, as described in chapter 3.4. Then, YOLOv4 is used to automatically detect large cavities in an image of a sample. This is done primarily to showcase the successful application of the elaborated workflow and to gain experience. Then, the verified workflow is used to detect the cover layers of these cavities and finally the network is trained to detect both, cavities and cover layers at the same time. To demonstrate the use of the workflow with more realistic image data, the network is finally trained to detect big cavities in images, showing the entire build job.

4.1.1 Image Analysis

Figure 4.1.1-1 shows the mean gray values of each layer averaged over all five C_{1000} samples. The first 69 images of each stack show the support structure, which is very delicate and not part of the design itself. Due to the small share of molten powder in each layer, the mean gray values of those layers are very low. The decreasing trend of the mean gray value towards the bottom and top of the support structure can be explained by the tapered design of the support structure (see Figure 3.2.3-2). The gray value peaks in layer 70, which is the first layer above the support structure, with a mean gray value of over 70. This peak is present in the data of all analyzed samples and therefore is not type-specific. It is caused by the rapid increase of energy supply and high share of unmolten powder in the underlying layer. This effect decreases fast within only a few layers. The abrupt rise of the gray value, due to high porosity in the layer underneath is the same effect, that was detected in earlier research in layers above very large cavities.

The layers of the remaining sample can be divided into sections with a mean gray value between 25 and 30 and sections with mean gray values below 25. In Figure 4.1.1-1 the correlation of the gray value and the design is very distinct. The sections of lower gray

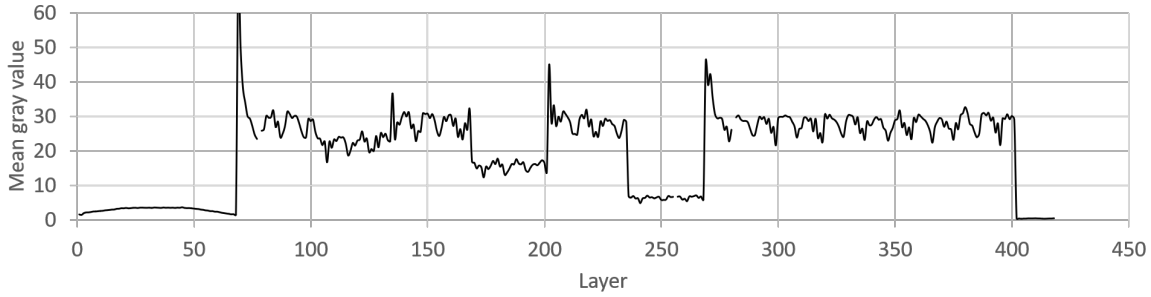

Figure 4.1.1-1: Mean gray values of all layers of five averaged C_{1000} samples.

values can easily be assigned to the cavities. The first cavity, between layers 101 and 134, has a diameter of 2 mm and the mean gray value only decreases slightly, but noticeably. The following cavities, increasing in diameter, show even greater decreases. The difference between the gray values in the section of the last cavity, which has a diameter of 4 mm, and the sections without cavities is roughly 4 times greater than the difference between the gray value in the first cavity and the sections without. This quadratic relationship is rooted in the quadratic relationship between the diameter and the area of a circle, see equation 4.1.1-2 and the linear relationship between the percentage of black pixels and the mean gray value in an image 4.1.1-3.

$$A_{Circ} = \Pi \frac{d^2}{4} \tag{4.1.1-1}$$

$$\psi_{Mean} = \frac{\sum_{i=0}^{N} \psi_i}{N} \tag{4.1.1-2}$$

(4.1.1-3)

As expected, the gray values in the layers directly above the cavities are very high and can be spotted easily in the diagram, as well as by comparing the cover layers to other layers. While the peak of the first and smallest cavity is significantly smaller, than the other two, the data in Figure 4.1.1-1 does not suggest that the mean gray value of a cover layer is proportional to the size of the cavity underneath, as the difference between the second and third cover layer is only minor. Nevertheless, the data does suggest, that cover layers should be detectable by computer vision.
In addition, it is noteworthy to observe that in the sections where no cavities appear, the data tends to oscillate periodically with a magnitude of roughly 4 and a frequency of about 9 layers. This effect is analyzed further in chapter 4.3.2.
The findings presented are supported by the analogous analyses of the C_{2000} samples. The corresponding diagram can be found in Appendix A.

4.1.2 Deep Learning

To achieve the first goal of accurate detection and localization of cavities in a layer, not the whole data set is necessary. To decrease memory space and computation time, the data set is reduced. Therefore layers showing support structures and IDs on top of each sample, are

not part of any data set used for training.
The second goal is the detection of not only layers showing cavities, but also detecting cover layers. This is an important step towards automatic detection of defects, such as cavities and cracks.

Cavities

First, following the recommendation of the developers of YOLOv4, a very large data set is composed to complete the task of detecting and localizing cavities. From the original data set, containing all layers of five C_{1000} and five C_{2000} samples, only those layers are selected, containing a cavity. All images therefore show a black circle in the center with a diameter of either 2 mm, 3 mm, or 4 mm. Using equation 3.3.2-1 and the information from the design (see Figure 3.2.2-1b), all layers showing a cavity can be selected easily. The data set is completed by adding an equal amount of images without cavities. In total this first data set consists of 2000 images.
The pretrained CNN is trained for only 1000 iterations and both average loss and mAP are recorded, depicted in figure 4.1.2-1. The average loss is very high at the very beginning but

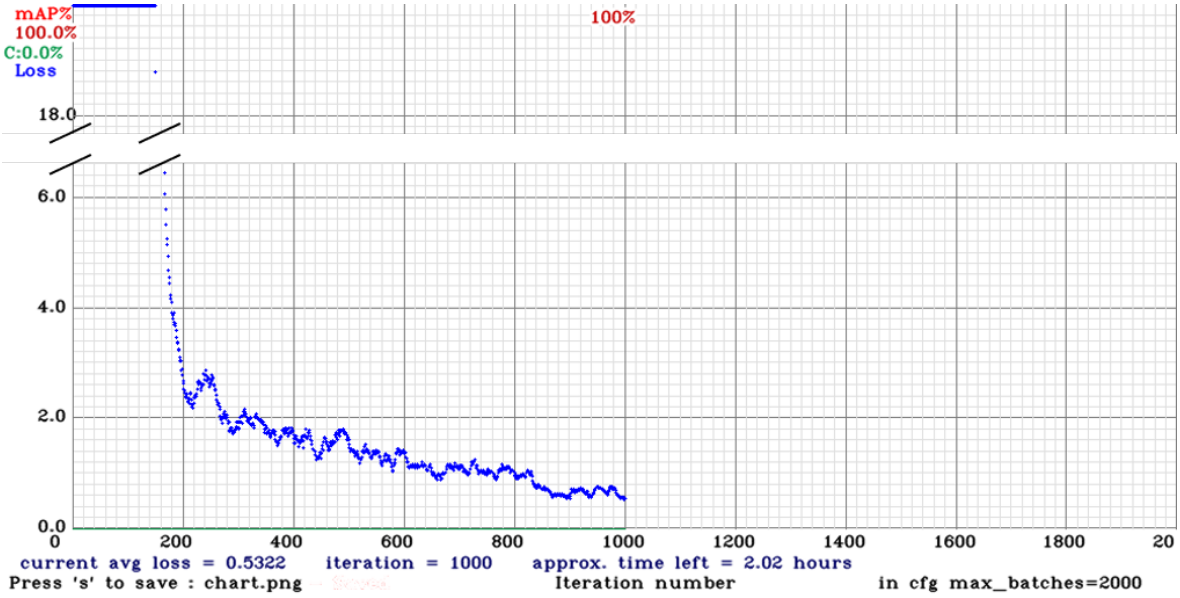

Figure 4.1.2-1: Mean average precision (mAP) and average loss over 1000 performed iterations of the neural network trained with data set *Big Cavities*

decreases exponential. After only 200 iterations the average loss is close to 2.0, the decrease then slows down and after 1000 iterations the average loss is close to 0.5. At this point is the minimum of average loss and a mAP of 100 %. The weights generated at this iteration are used for testing.
Figure 4.1.2-2 shows the results of the CNN with multiple test images. The three images to the right next to the image stacks show the correct localization of cavities, more or less identical to the training data. However, the test images are neither part of the training nor the validation data set. The bounding box in framing the 2 mm cavity at the bottom is very accurate and tight. The bounding boxes framing the 3 mm and 4 mm cavities are

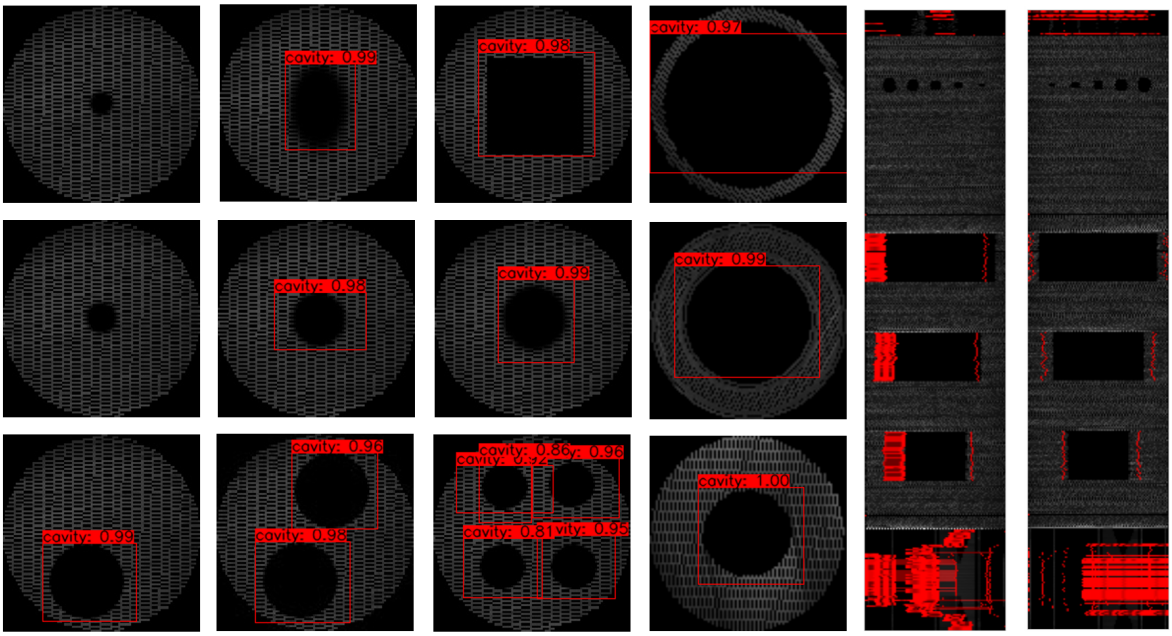

Figure 4.1.2-2: Detection of selected testing data with a *Big Cavities* trained NN. On the right two sectional views of a complete sample stack.

slightly to flat, not framing the entire cavities as a result. The classification shows very high confidence for all three cavities between 97 % and 100 %. These results are not surprising, as the difference between the training data and testing data is more or less not existent.
To test the network for over-fitting, which is likely to occur due to the small variety of training images, more testing data is generated by basic image editing. Generated images with smaller black circles in the center of the image show limitations of the network. The two images on the left of the 3 *mm* cavity show accurate detection with high confidence of the circles with diameters of 1.5 *mm* and 1 *mm*. However, the even smaller circles in on the very top and middle left with diameters of 0.75 *mm* and 0.5 *mm* are not detected. There are at least two possible reasons for this. As presented in chapter 3.1.2, YOLOv4 provides a set of built-in data augmentation techniques which is used in training and one of these techniques is random scaling of the input images. However, the scaling factors are limited and therefore only changes in size of the object to a certain degree are possible. Another potential reason is, that the size of the object is too small to be detected due to architectural limitations of the CNN. The authors of the code advice users to adjust the architecture, if very small objects are to be detected, but state that objects larger than 16 *px* by 16 *px* in a rescaled 416 *px* by 416 *px* image invalidate this necessity. Furthermore, following results show successful detection of even smaller cavities. It is therefore very likely, that the observed limitations are caused by the small diversity of the data set and limited scaling factors of the used data augmentation.
To further test the limits of the built-in data augmentation techniques, more test images are generated, including images with multiple cavities and non-centered cavities at the bottom and cavities with various shapes, like rectangles and ovals in the top row. The results demonstrate the strength of data augmentation during training, as almost all cavities are detected with very high confidence. Only in the image with four circles there are two bounding boxes

framing the same circle in the top left. If the goal is to detect objects and not count their number, this type of error is neglectable.
To test the reliability of the network, a complete image stack of a C_{1000} sample, that is not part of the data set used for training, is tested. To visualize the results, the new image stack, including the bounding boxes in red, is cut in half along the xz plane and along the yz plane, both depicted on the right hand side in Figure 4.1.2-2. This representation allows two major observations.
Firstly, in the layers of the support structure in the lower part and the layers of the sample ID a great amount of cavities is detected. Structures that remotely resemble black geometries, like circles or rectangles, are falsely recognized as cavities. As mentioned, these layers are not part of the training data set at all and share only minor similarities with the actual training data. To prevent these kind of errors, the training data set should be extended by as many images, showing any kind of possible structures.
Secondly, it can be observed that the bounding boxes, framing a cavity of a certain diameter, all have very similar sizes and positions. This becomes particularly clear, looking at the uppermost and largest cavity of the three. As previously noted,the framing of the bounding boxes is not fully satisfactory, which is clearly visible. The sectional views of the image stack reveal, that this error is present in every layer of this cavity and the characteristics of this error are very similar. The cause for this is likely to be found in automatic labeling of the data set, which, again, is not very diverse. Automatic labeling of the data set, as done in this work, leads to passing on of errors and further shrinking of diversity, as simply the same position and size of bounding box is copied for all images. Because cavities of different size and shape, not present in the training data set, show more fitting bounding boxes, the error is suggested to be caused by overfitting due to automatic labeling. In chapter 5.2.2 a workflow improvement is suggested to prevent this behavior.

Data set size reduction Because the images are all very similar, the great amount of data used is judged to be exaggerated and even causing errors by overfitting, as discussed. To research the necessity of large amounts of data, as recommended by the developers of YOLOv4, when the objects are very simple and the diversity of the data is very small, a second, much smaller data set is composed. This reduced data set only consists of 60 images in total: 10 images of cavities with 2 mm diameters, 10 with 3 mm diameters and 10 images showing cavities with 4 mm diameters. The remaining 30 images are layers showing no cavities. Again, a pretrained YOLOv4 CNN is trained with the new data set. The same amount of iterations (2000) is performed and the weights with minimal average loss are chosen. This allows a comparison between both data sets.
Testing the trained network is done with the exact same testing images, as for the larger data set and results are depicted in Figure 4.1.2-3. Two major observations can be noted: The impact of the very significant reduction of the image data is rather low and smaller objects are even detected with higher accuracy. But on the other hand the already observed error of repeated detections of an object is present more often.
This supports the suggestion, that diversity of the data set is more import than size which can even harm the quality of the network by overfitting. The issue of same sized and positioned

bounding boxes can be seen here, too. This reinforces the assumption that lack of diversity through automatic labeling is the cause of this.

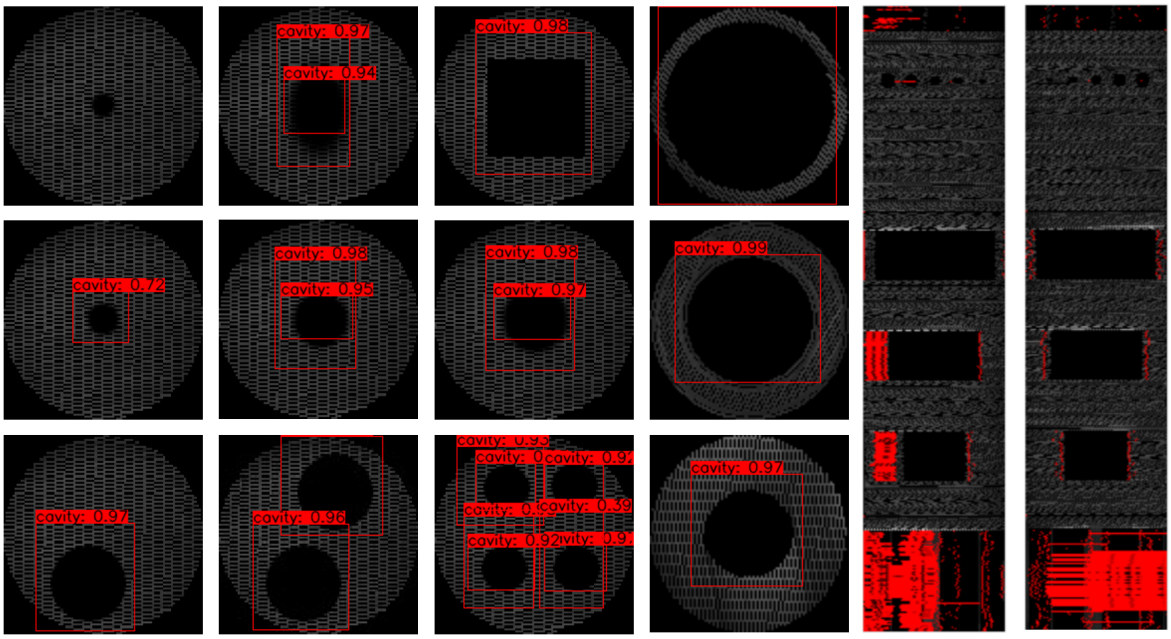

Figure 4.1.2-3: Detection of selected testing data with a *Big Cavities - Reduced* trained NN of only 60 training images. On the right two sectional views of a complete sample stack.

Covers

Following the successful demonstration of the workflow and convincing results even with a very small data set, a subset is composed with only images showing the covers of large cavities. The quantity of such images in the data set is much smaller than of images showing a slice of a cavity. Considering all manufactured samples of type C_{1000} and C_{2000}, a training data set is created containing 24 cover layers with 2 mm and 4 mm cavities underneath and 10 cover layers with 3 mm diameters underneath, as those only appear in C_{1000} samples. For the computation of the mAP, a validation data set and for testing one more data is generated with 2 images per diameter each. In all three data sets the number of labeled images is matched by images showing layers that are neither cavity- nor cover layers.
Figure 4.1.2-4 shows a very fast decrease of the average loss below 2.0 in only 200 iterations. The value than decreases nearly linear, again the network is trained for 2000 iterations. The graph shows potential of further decrease of average loss for more iterations. The mAP is at 100 % for most iterations, but shows a deep sink down to 67 % at iteration 1600. The magnitude of this deflection is caused by the very small quantity of the validation data set consisting of only 12 images in total. For testing the weights gathered at iteration 2000 are used, as they show the lowest average loss.
First, the network is tested with the composed testing data set. Figure 4.1.2-5 shows the results of the six testing images of cover layers. All cover layers are classified as such and none of the non-cover layers in the testing data set are falsely classified. However, the predictions are not very accurate. Especially for the cover layers of smaller diameters (2 mm on the

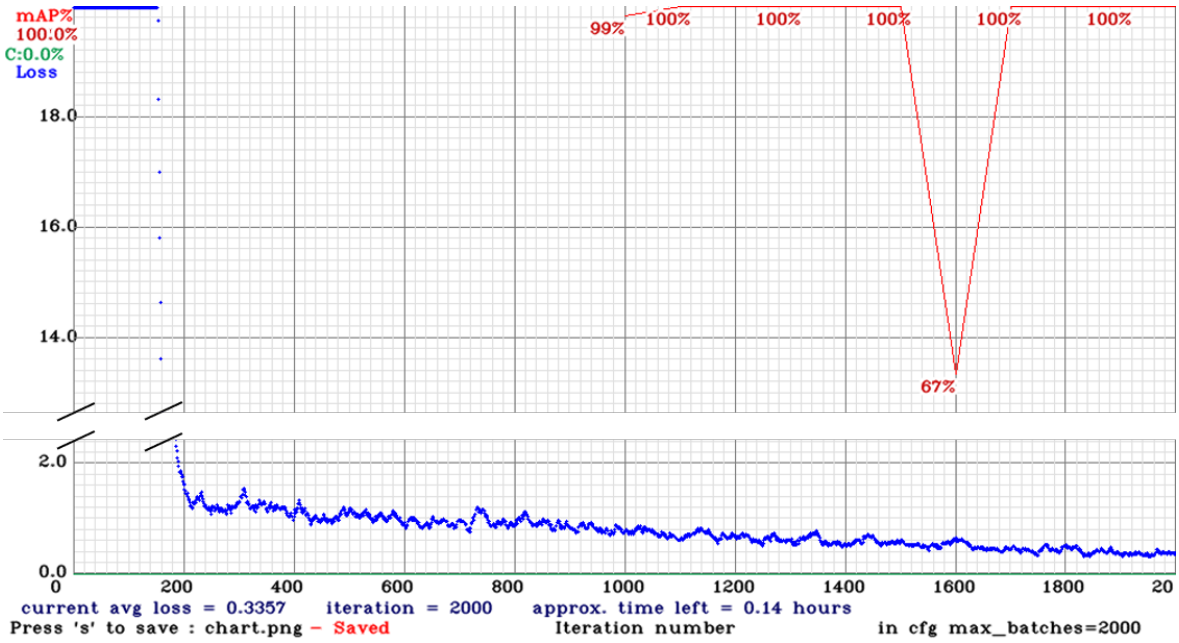

Figure 4.1.2-4: Mean average precision (mAP) and average loss over 2000 performed iterations of the neural network trained with data set *Big Cavities - Covers*

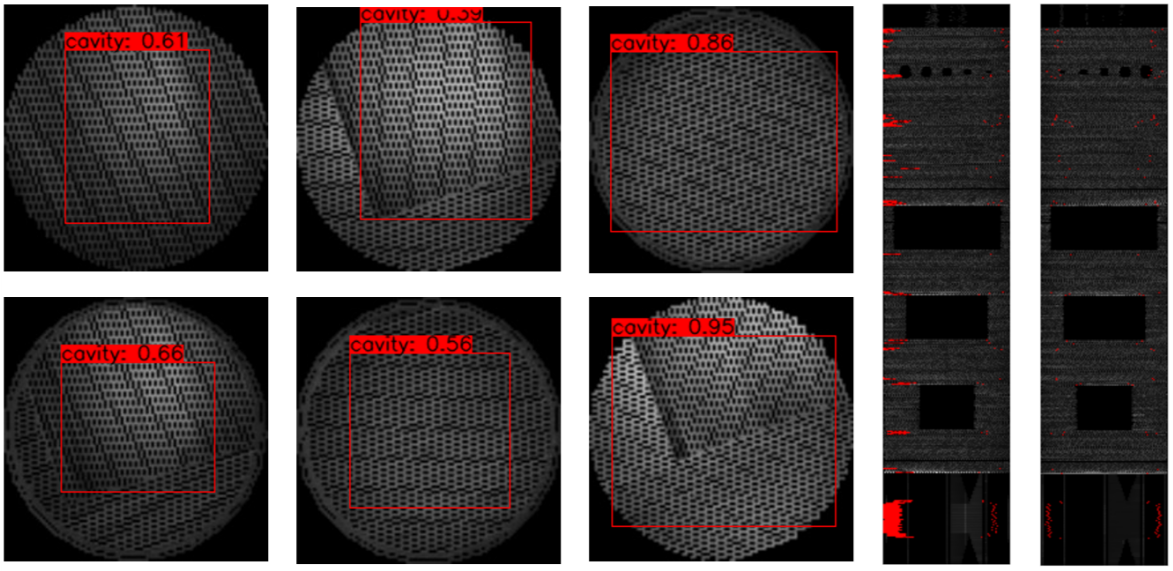

Figure 4.1.2-5: Detection of selected testing data with a *Big Cavities - Covers* trained NN. On the right two sectional views of a complete sample stack.

left and 3 *mm* in the middle) confidence values are only between 39 % and 66 %. The two 4 *mm* covers on the right show higher confidence values of 86 % and 95 %. However, neither the data set used for training nor the one used for testing are large and diverse enough to provide a sound assessment of the reliability and accuracy of the network. This is supported by testing the image stack of a complete C_{1000} sample. Again, layers of the support structure are falsely classified. Also, the sectional view shows that a large amount of layers are falsely classified. Classification of the first layer above the support structure is not surprising, as this layers shares the key characteristic of high mean intensity (see Figure 4.1.1-1). Moreover, the classification of layers underneath cavities is striking. However, the regular appearance of further falsely classified layers in the upper part of the sample does not allow to draw conclusions whether layers below cavities share characteristics with those above, or if those characteristics are shared by layers in a certain pattern, for example due to the chosen scan strategy, which seems to be more likely.
In summary, detecting cover layers is assessed as possible using the elaborated workflow, although building a larger data base is considered necessary to improve predictions and allow further research.

Cavities and Covers

Lastly, the small data set for detection of cavities and the data set for covers are combined and YOLOv4 is trained to detect both large cavities and their covers. As depicted in Figure 4.1.2-6, the same observations can be made, as for the data sets on their own. The training of both classes at the same time seem not to effect the results significantly.

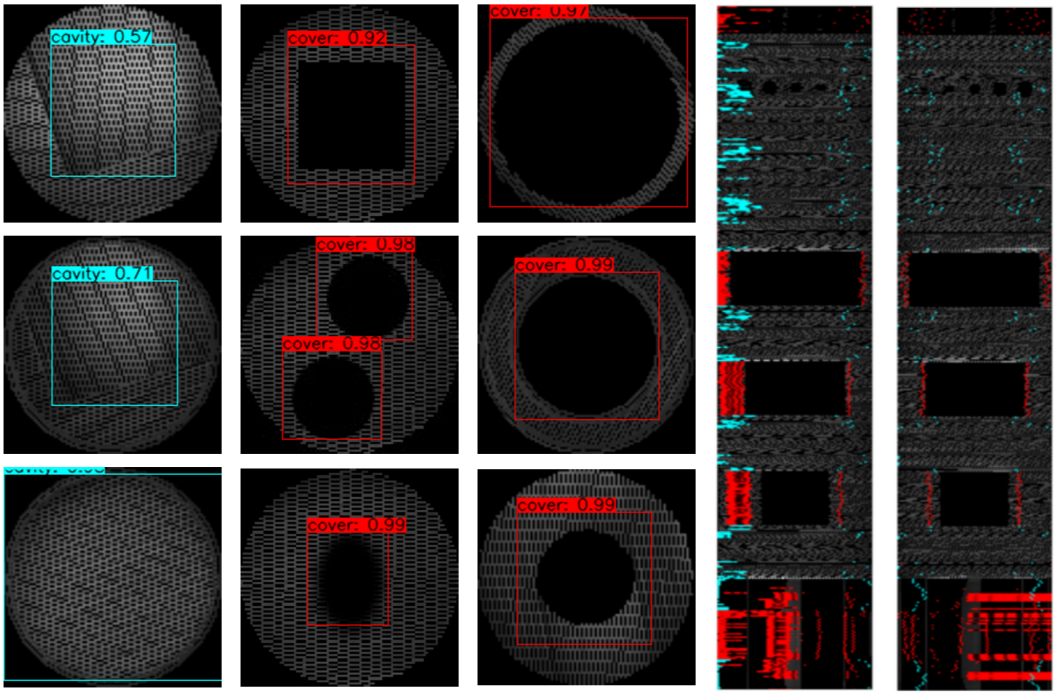

Figure 4.1.2-6: Detection of selected testing data with a *Big Cavities - Cavities+Covers* trained NN. On the right two sectional views of a complete sample stack.

Build Job

Furthermore, a data set is composed to test detection of large cavities in a more realistic scenario. All networks discussed previously consist of only images showing one single sample. Considering the application of an automatic defect detection network, the entire build volume should be trained. As build times decrease due to new machine designs offering simultaneous use of multiple lasers and higher efficiency, evaluation of an entire layer of the build job is considered mandatory. To proof the capability of the developed workflow, a data set is composed showing the entire build job. As for the data set with single samples, all large cavities are labeled and a pretrained YOLOv4 CNN is trained. Using a resolution of 250 μm, the images have a size of about 1050 px by 1050 px.
In Figure 4.1.2-7 the detections in one testing image are shown. On the left, the entire build job is depicted showing correct detection of all 18 artificial cavities present with confidence value between 85 % and 97 %. On the right a close up of the TL segment is shown. This shows, that the presented workflow is suitable to detect objects like cavities of a size of at least 2 mm in diameter by processing the entire build job in each frame. With the near real-time speed of YOLOv4 each layer can be processes multiple times during production and defects can be detected immediately. This could proof useful especially when detecting major defects, which could potentially harm the machine and risk termination of production.

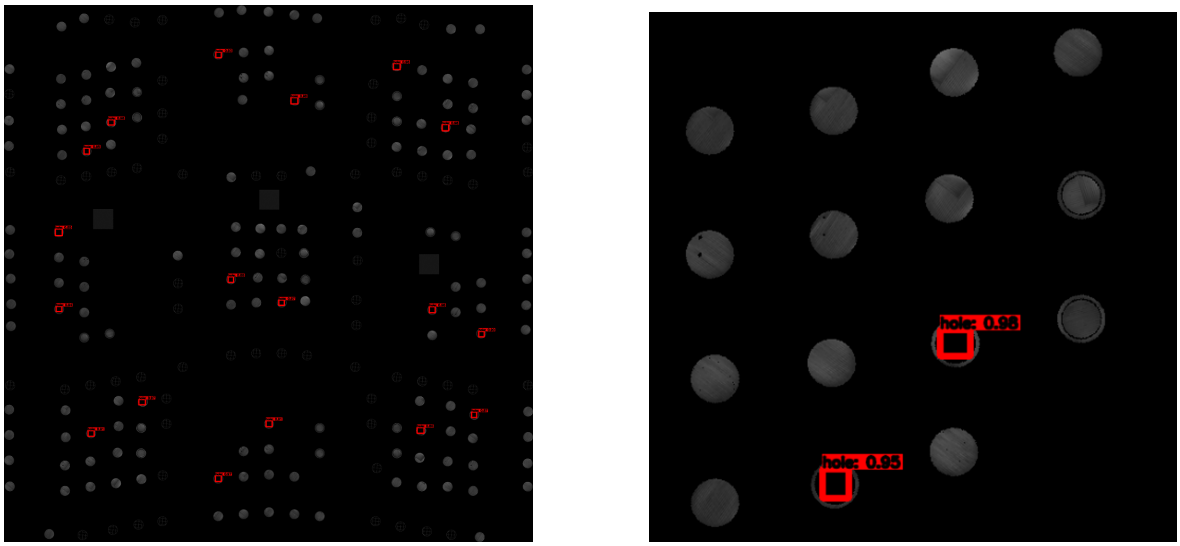

(a) Entire build job

(b) Close up of the TL segment

Figure 4.1.2-7: One layer of the entire build job with 18 artificial cavities with 4 mm diameters present which are all detected

4.2 Data set *All Cavities*

For the second data set, samples of type C_{1000}, C_{2000}, C_{60}, S_2 and P_5 are selected. With a much broader set of objects of various sizes and shapes it is expected to achieve a network to detect a larger variety of cavities and especially is capable of detecting smaller objects.
As for the first data set, first the data is evaluated by computing mean intensity values and

afterwards Deep Learning is used to detect cavities both in the layers of their appearance in the layers right above.

4.2.1 Image Analysis

Analogous to the analysis of C_{1000} and C_{2000} samples, this research is focused on the correlation of the sample design and the gathered MPM-data of each sample type.

PVar

Even though the P_{Var} samples are not part of the data set used for Deep Learning, analyzing this type is especially interesting, as the size of defects and porosity changes along its z-axis. In figure 4.2.1-1, showing the mean gray values averaged over all P_{Var} samples with 2 mm supports, one can observe the distinct sinks of the gray value in layers with cavities present. These sinks increase in magnitude with increasing size of the cavities and therefore the percentage of black pixels. The first cavity layer, containing cavities with a diameter of only 30 μm does not show a significant decrease of the mean gray value, as it exceeds the chosen resolution of 50 μm. However, the peaks in the cover layers, characteristic to the previously analyzed C_{1000} samples, are not present in the shown data. To further investigate the gray values in the cover layers the maximum gray values are analyzed, as peaks should be more prominent, but no significant correlation can be found. In addition to the MPM-data,

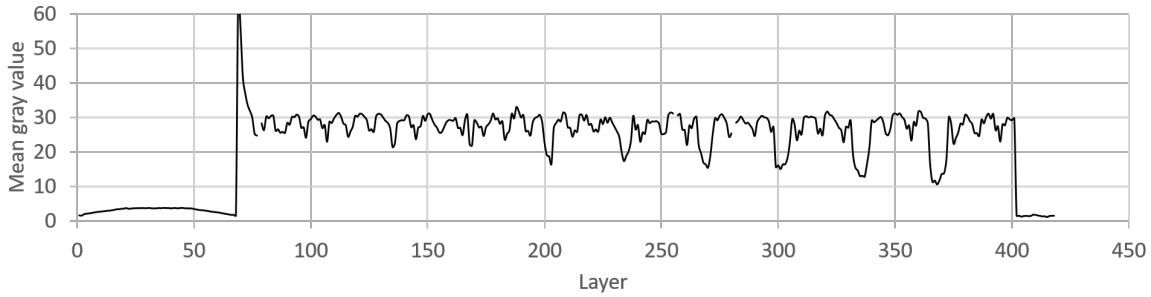

Figure 4.2.1-1: Mean gray values of all layers of five averaged P_{Var} samples.

a P_{Var} sample is analyzed using CT. This allows to investigate the resulting cavities in the samples. Using the Software *Avizo*, the cavities are extracted from the CT-data. Figure 4.2.1-3a shows the CT-data, correlated with the MPM-data and the CAD-data. The colors in the CT-data represent the position of the cavities, so that they can be easily assigned to the corresponding layer. Cavities in the top four layers (180 $\mu m \leq d_C \leq$ 270 μm) can be clearly distinguished as designed cavities from natural defects, which occur significantly more often in the direct neighborhood of the former, see figure 4.2.1-3b. For the cavity-layers below ($d_C \leq 120$ μm) the size of artificial cavities and natural defects become more and more similar. Cavities with a diameter of 90 μm and 60 μm can not be distinguished, except by their position in the sample. The cavities with diameters of 30 μm are neither detectable in the CT-data nor in the MPM-data. However, even large cavities show great deformation. Comparison of the three data types shows that even for the uppermost cavity layers with

very large cavities and high porosities, there is no significant effect observable in the cover layers of the MPM-data.

P5

The same studies are performed for a P_5 sample, see figure 4.2.1-2 and figure 4.2.1-3. As for the P_{Var} sample, CT shows detectable cavities for diameters of at least $d_C = 120\ \mu m$. Observations regarding the deformed shape of the cavities are validated, but the amount of natural defects is significantly lower. The mean gray values show slight decreases in the cavity layers,

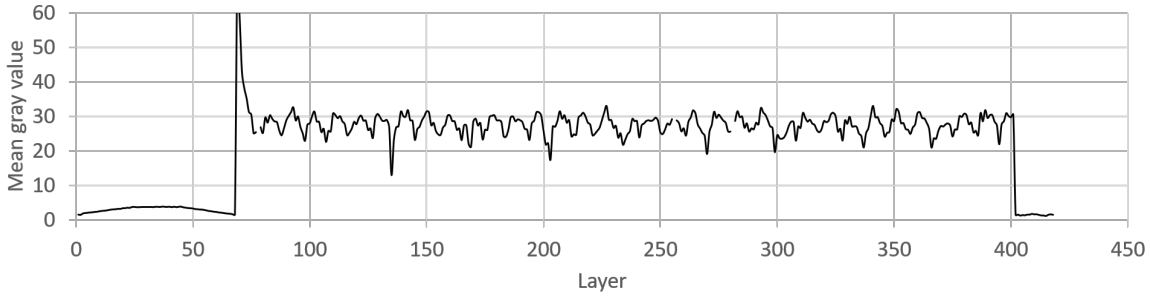

Figure 4.2.1-2: Mean gray values of all layers of five averaged P_5 samples.

but again significant peaks in the layers above are missing. Figure 4.2.1-3d shows accurate formation of most cavities with diameters greater than 150 μm. However, some cavities are missing in the CT-data. Especially in the layer of cavities with diameters of 180 μm colored in blue a lot of cavities are either missing or very small. This demonstrates that creating very small spherical cavities with high accuracy is not trivial, even with optimized parameters.

C60 and S2

Additionally, the mean gray values of C_{60} and S_2 samples are analyzed, shown in Figure 4.2.1-4. Both show neither peaks in the cover layers nor sinks in cavity layers. However, the oscillation, also present in all other analyzed data is very striking. Comparing both graphs not only the frequency of the oscillation seems to be same, but also the phase. Further investigation is presented in chapter 4.3.2. Looking at the images of the two stacks, the layers with cavities present can be distinguished from the rest easily by the human eye. This indicates that analyzing the mean gray value is only useful for very large cavities and missing events in the graphs does not necessarily mean that the images do not provide information. This could also apply for cover layers, even though they can not be distinguished by the human eye.

4.2.2 Deep Learning

As for the data set *Large Cavities*, the data set is reduced in size by excluding all layers below and above each sample. And again, first a YOLOv4 CNN is trained to only detect the cavities and only after that the detection of cover layers is aspired.

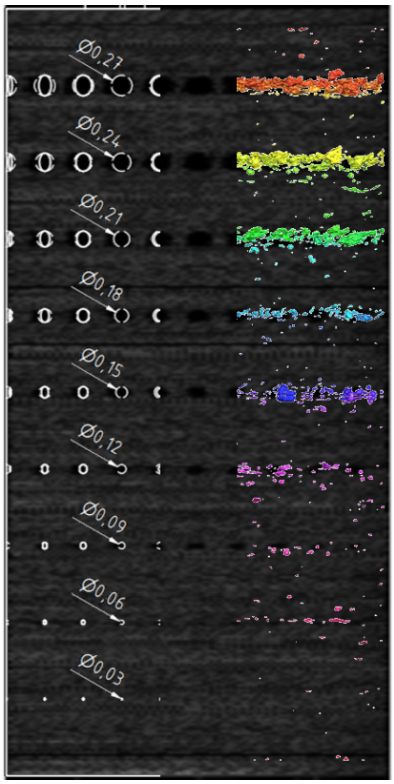

(a) Correlation of MPM-Analysis (bw backdrop), CT-Data (right) and Design (left) of a P_{Var} sample.

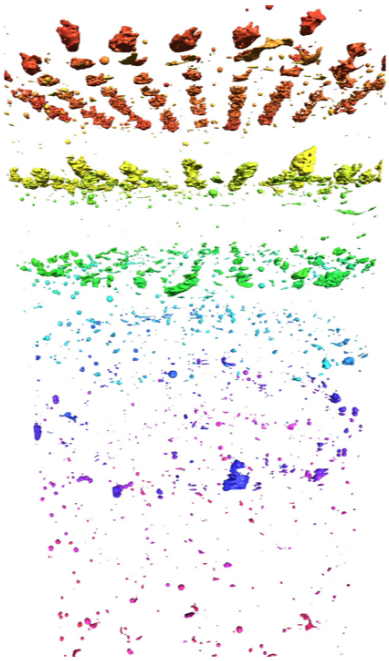

(b) Cavities extracted from CT-data, perspective shows the individual cavities in each layer.

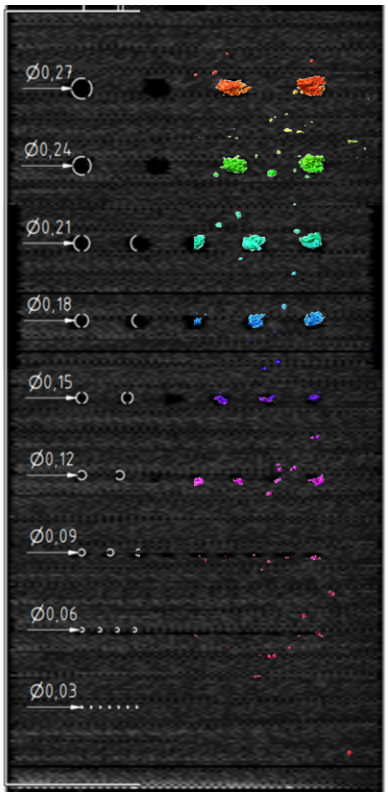

(c) Correlation of MPM-Analysis (bw backdrop), CT-data (right) and Design (left) of a P_5 sample.

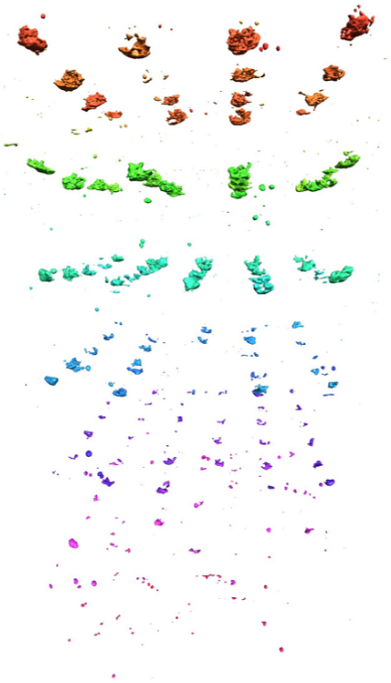

(d) Cavities extracted from CT-data, perspective shows the individual cavities in each layer.

Figure 4.2.1-3: CT-data of a P_5 and P_{Var} sample correlated with MPM- and CAD-data. Cavity layers are distinguished by colors.

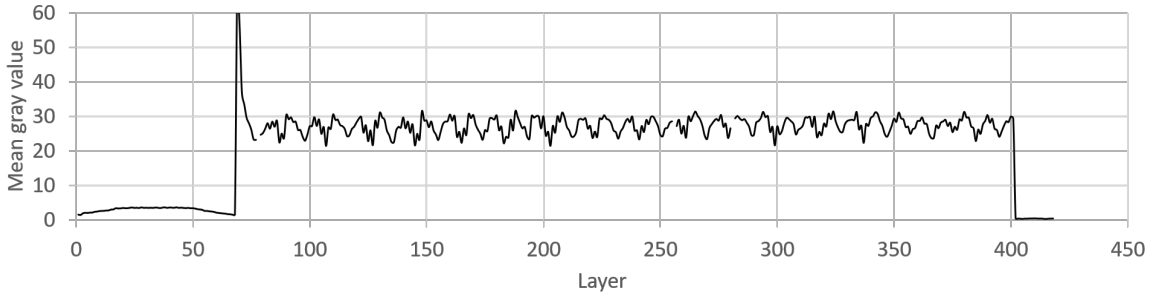

(a) C_{60}

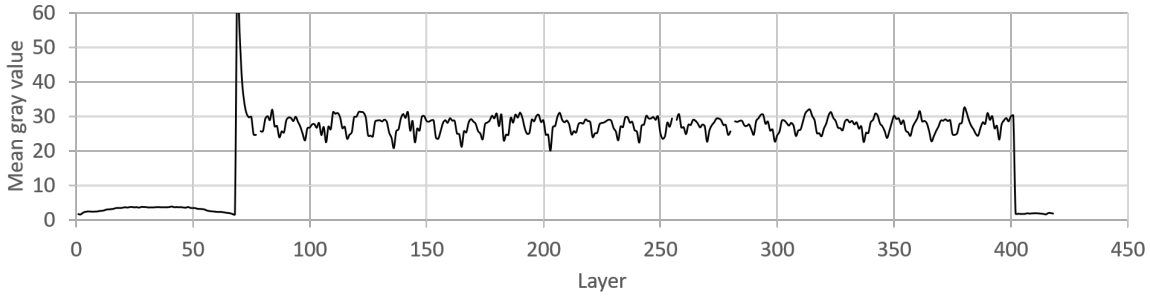

(b) S_2

Figure 4.2.1-4: Mean gray values of all layers of five averaged samples.

Cavities

Taking into account the experiences gathered in training the network with the data sets previously, this new data set consists of a maximum of ten images showing the same set of cavities to prevent overfitting. Therefore, 40 cavity layers are selected from both C_{60} and S_2 samples each, as there are four different cavity layouts. Adding to those 80 images, 30 images from C_{1000} samples are chosen. From P_5, 10 images per layout are selected. Again, the total amount of images showing cavities is matched by images showing layer without any cavities present. And as before, the data set is divided into a training and validation data set. For validation, 2 images of each cavity layout are selected.

Figure 4.2.2-1 shows the mAP and average loss over the computed iterations. In total the network is trained for 2000 iterations. Due to the higher diversity of the data set and wide range of bounding box sizes, the average loss decreases much slower. After 1000 iterations the average loss is at about 5.0 and the first calculated mAP is at 91 %. The mAP increases during the following 300 iterations and settles at 94 %, while the average loss decreases further and falls below 2.0 after more than 1600 iterations and a minimum is reached after 1900 iterations at 0.98. The last 100 iterations show an increase of the average loss.

The network is tested with images showing both real and edited cavities, a selection, including a complete S_2 stack, is shown in Figure 4.2.2-2. Overall, both the accuracy of the bounding boxes as well as the confidence of the predictions are very high. Except for some of the many cavities in a layer of a P_{Var} sample, all cavities are detected and only some oval cavities are detected multiple times, as observed previously. Despite trained with less images showing large cavities, the bounding boxes framing those are more tight and confidences are very high. This very successful demonstration shows the capabilities of the presented workflow with only

limited amounts of data. This is particularly gratifying, as the previous gray value analysis was not capable of detecting cavity layers.

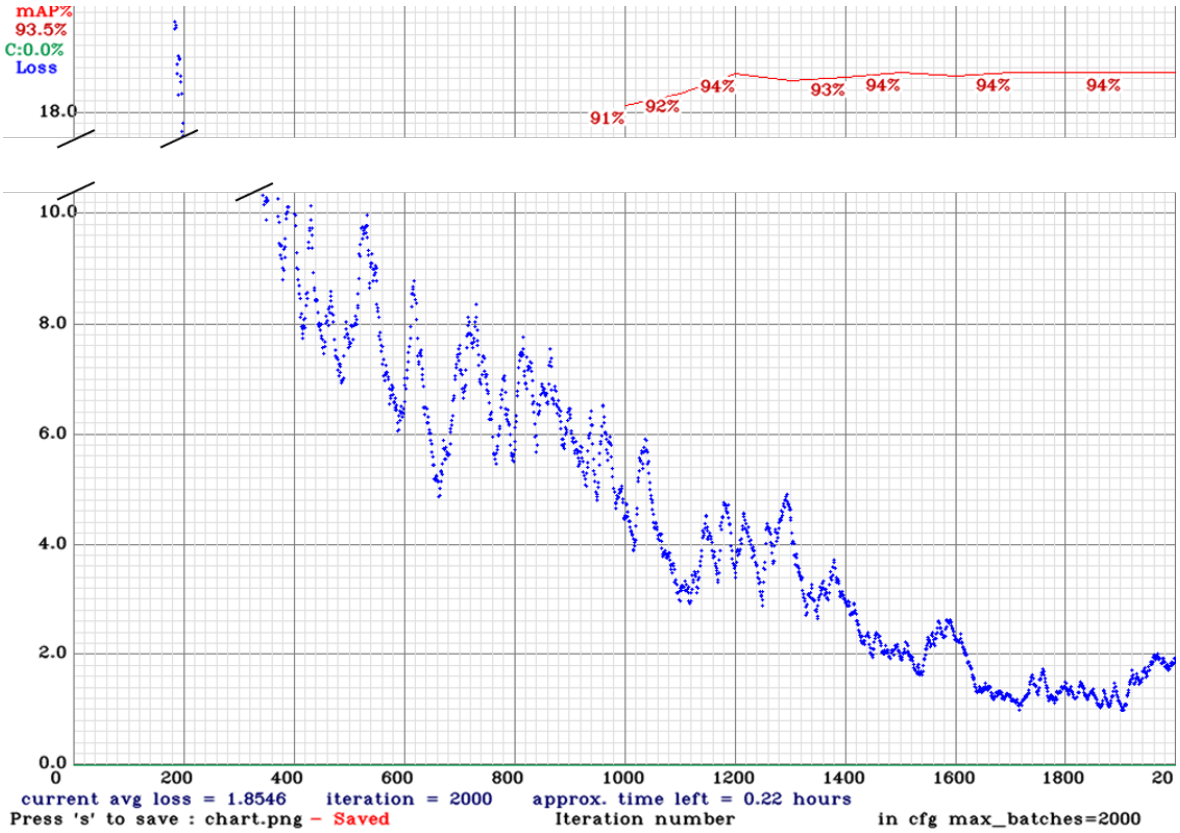

Figure 4.2.2-1: Mean average precision (mAP) and average loss recorded during training of the *All Cavities* data set over 2000 iterations.

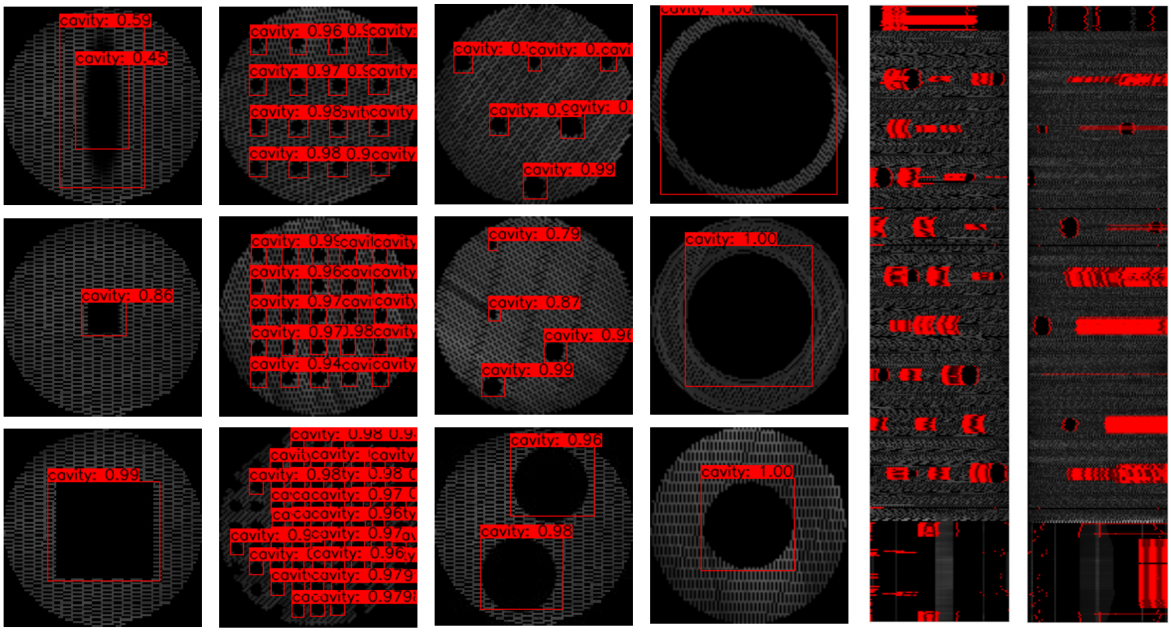

Figure 4.2.2-2: Detection of selected testing data with a *All Cavities* - *Cavities* trained NN. On the right two sectional views of a complete S_2 sample stack.

Covers

As for the data set *Big Cavities*, following the successful demonstration of detecting cavities in-plane, a data set is generated that consists of only cover layers of those cavities. For this all cover layers of the previously trained cavity layers are selected and labels are simply copied. This can be done, because the location to be detected is equal to the location of the cavities in the layer beneath the cover layer. As before, the network is trained for 2000 iterations. Figure 4.2.2-3 shows the mAP and average loss over the trained iterations. In contrast to previous diagrams, both mAP and average loss show a different course. First, the

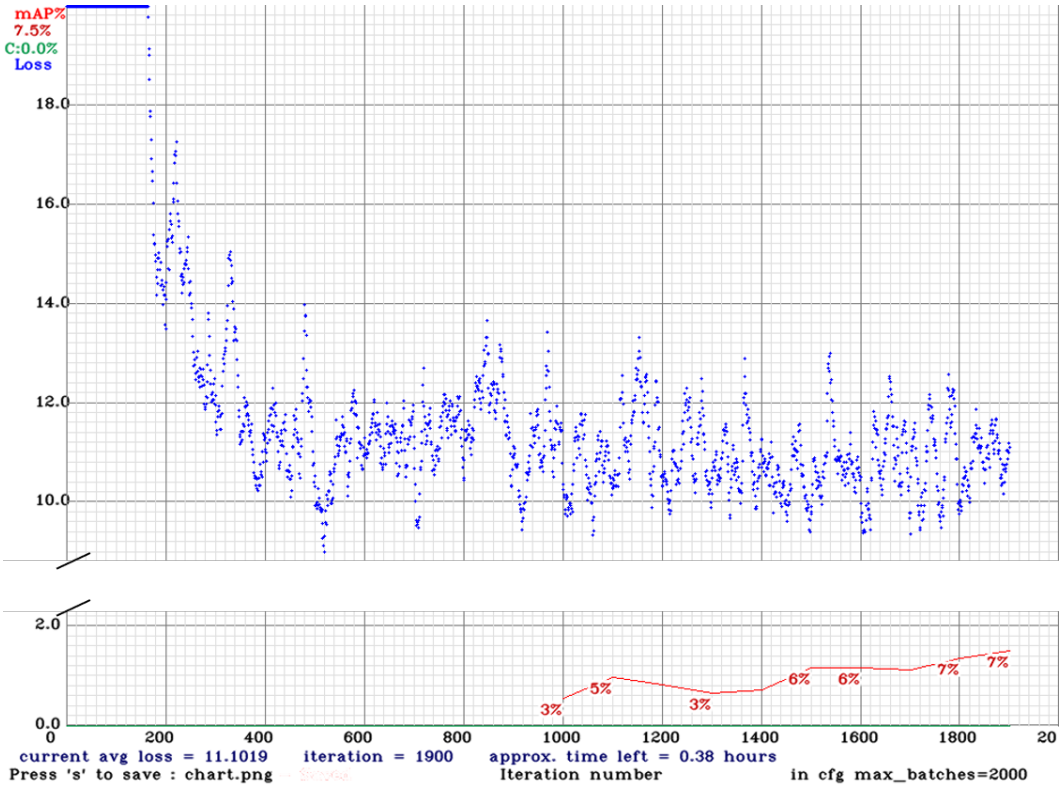

Figure 4.2.2-3: Mean average precision (mAP) and average loss recorded during training of the *All Cavities - Covers* data set over 2000 iterations.

average loss decreases as expected, but stops to decrease at around an average loss of 14.0 after 200 iterations. Then strong oscillation of the loss can be seen. This oscillation shows a magnitude of about 2.0 and a more or less constant mean value of 11.0 after 600 iterations. The mAP, measured with the validation set, starts at 3 % after 1000 iterations and increases only slightly to about 7 % after 1900 iterations.
These results clearly show unsuccessful training. Both graphs do not suggest that significantly better performance can be expected, if trained for more iterations. This behavior is likely to be rooted in either the gathered data, simply not providing the necessary information, or in the developed workflow, not handling the collected data in a way the necessary information can be detected. While the latter is difficult to proof, as this would require extensive parameter studies, the former is further investigated to be able to better judge the quality of the gathered data.

4.3 Parameter Analysis

In the following, the effect of the chosen process parameters and the influence of the scan strategy are discussed. To do so, first the mean gray values of samples manufactured with different parameter sets are compared. Then, measurements of a parameter stack sample are examined and finally the oscillating nature of the investigated mean gray value is investigated briefly.

4.3.1 Influence of volume energy density

Figure 4.3.1-1 shows the mean gray values of all averaged N_1, N_2 and N_3 samples. It can be

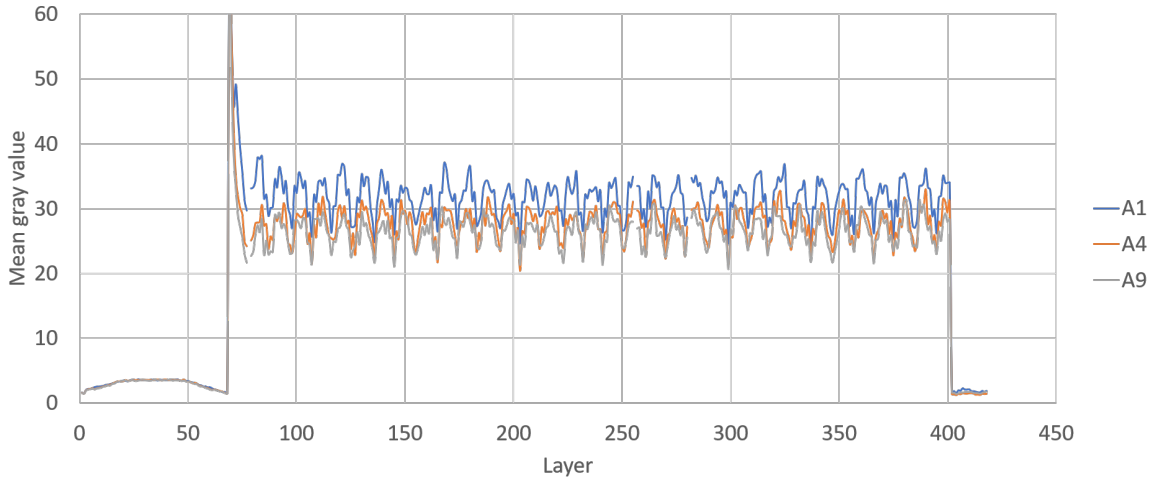

Figure 4.3.1-1: Mean gray value of all layers of five averaged N_1, N_2 and N_3 samples each.

seen that the gray value of the N_1 samples made with parameter set A1 is higher than that of the other two samples. Furthermore, there is a slight tendency that the gray values of the N_3 samples manufactured with A9 parameter set are slightly lower than those of the N_2 samples manufactured with the standard A4 parameter set. These results correlate with the volume energy densities of the selected parameters ($E_{A1} = 292\ \frac{J}{mm^3}, E_{A4} = 117\ \frac{J}{mm^3}, E_{A9} = 58\ \frac{J}{mm^3}$). Figure 4.3.1-2 shows the linear relationship between the average of the layers $100 - 350$ of a sample type and the volume energy density of the parameter set used.

Together with the findings of Kasperovich et al. [19], which showed a nonlinear correlation between volume energy density and porosity, the generated porosity can thus be indirectly derived from the MPM data. However, the data show, as already discussed, significant oscillation around the mean value. The amplitude of these oscillations is so large that statements about the generated porosity do not seem possible without evaluating the data of several successive levels. Other influencing factors, such as the layer construction time, have much greater influences. This is impressively shown in figure 4.3.1-3b, where the gray values of a parameter stack sample are plotted. In the lower part of the samples between layer 0 (lowest layer of the sample) and layer 350 an expected course can be seen. The shown parameter stack sample was manufactured in the parameter sequence A4-A1-A9-A4-A1. Correspondingly, the mean value increases significantly after 100 layers and decreases again after 200

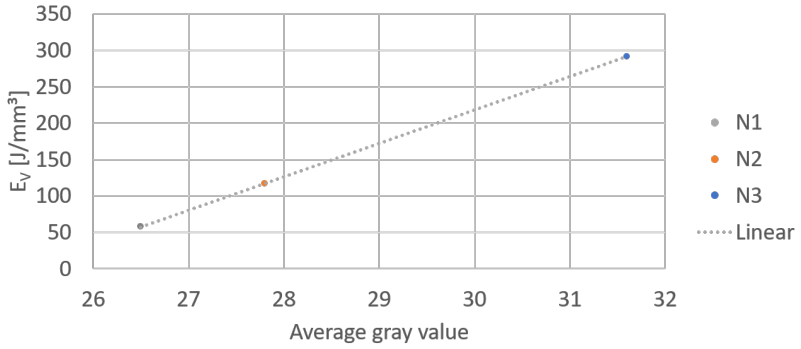

Figure 4.3.1-2: Averaged gray values of layers 100-350 of sample types N_1, N_2 and N_3 in relation to the volume energy density of the corresponding parameter set with dotted linear trend line.

layers, only to rise again after 300 layers, which is initially hardly measurable. After 330 layers, however, a significant increase is again visible. The values in the layers above layer 400 are also significantly higher than in the layers between 100 and 200, in which the same parameter set was used. This increase can be explained by the significant reduction of the layer building times between layer 330 and layer 340. Since the parameter stack samples with a total height of 15 mm are 5 mm higher than the remaining standard samples, only the 4 parameter stack samples are manufactured in the last 150 layers. This is accompanied by a significant reduction of the layer building times, which leads to a significantly lower cooling of previously produced layers. The reflected laser light therefore has a significantly higher intensity. These results show a serious influence of the layer building time on the energy applied and the resulting component quality. This manifests itself in significant deformations in the upper part of the sample as well as in very large pores, which are visible in the CT and can be clearly seen in figure 4.3.1-3a.

4.3.2 Influence of scan strategy

In order to examine the oscillation, which is found in all data, the gray value of the N_1 and N_2 samples in a selected area is plotted over 21 layers in figure 4.3.2-1. As already noticed before, the frequency as well as the phase of the oscillation is the same in all data. It can be seen that the oscillation period is approximately 10 layers. This indicates that the root of this phenomenon lies in the chosen scan strategy. The pattern of the scan vectors changes in each layer and the data indicates that a certain pattern is repeated approximately every 10 layers and that there are patterns that produce lower and those that produce higher mean gray values. At first, however, only the gray values can be determined, but not the energy input. The chosen visualization, resolution, or evaluation cannot be excluded as the reason for this anomaly. For this further work is necessary.

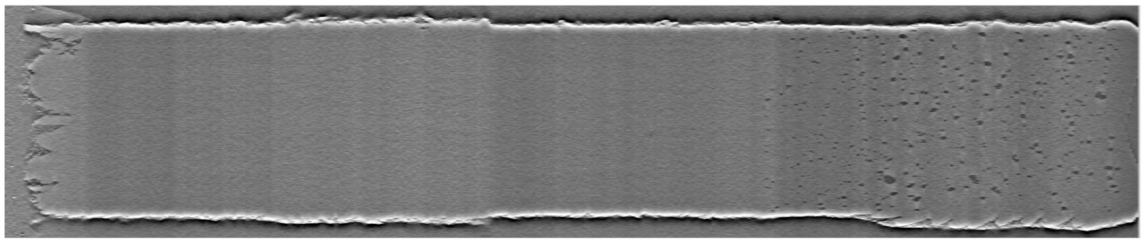

(a) Sectional view of a CT image stack. Parameter sections can be distinguished by eye, as higher energy input leads to deformation and higher porosity especially towards the top of the sample on the right.

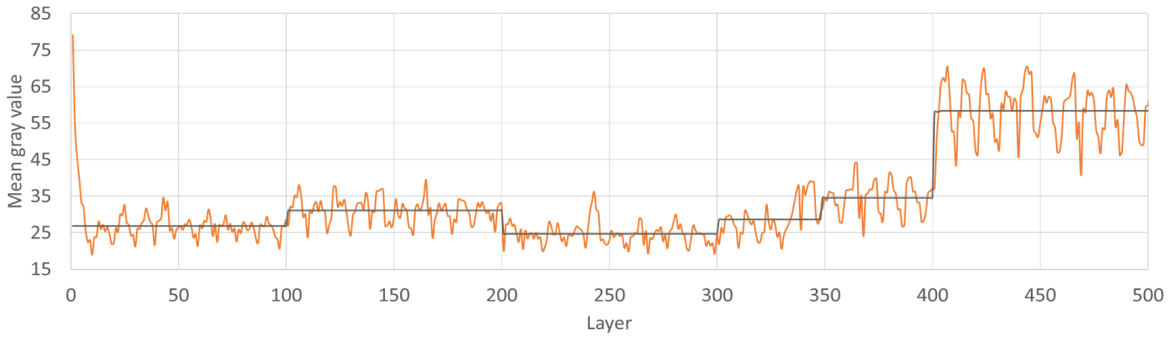

(b) Mean gray value of all layers of a parameter stack sample colored in orange. Averaged values of 100 successive layers colored in black (exception between 300 and 400).

Figure 4.3.1-3: Parameter stack sample with parameter set sequence: A4-A1-A9-A4-A1.

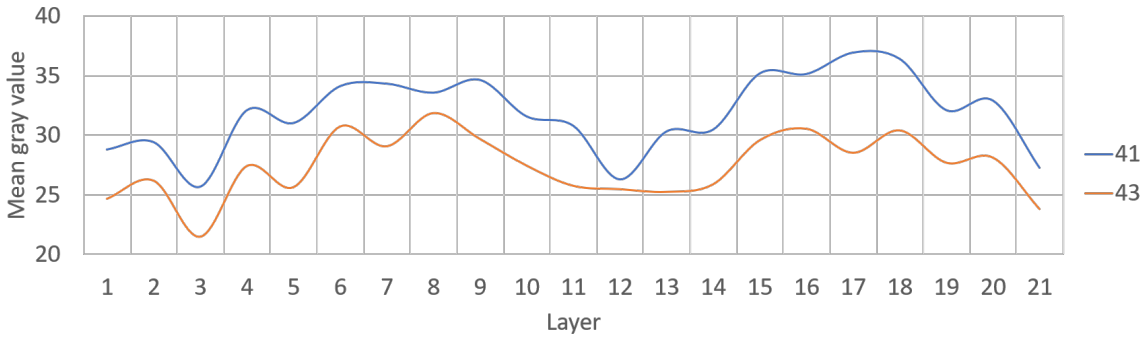

Figure 4.3.2-1: Mean gray value of selected layers of five averaged N_1 and N_2 samples each, showing the oscillating nature of the data with a period of 10 layers.

4.4 Evaluation of the Workflow

In principle, the application of the presented workflow for defect detection could be demonstrated. The presented results show that special events in the data can be detected and labeled precisely. However, the developed workflow also shows some limitations. Based on the processed data, no reliable statement can be made that cover layers of small cavities can be detected. In the following investigations it should be investigated if this is a limitation of the data or if the workflow can be further optimized. The use of the workflow required manual operations in many steps, which were particularly time-consuming. These included in particular labeling, which could be partially automated, but still required a lot of manual transfer of measurements. The results also showed that automating this process led to overfitting. Since a CNN is used to process image data, many post-processing steps are necessary to generate usable input data. This postprocessing significantly reduces the data content. A more direct use of the data measured by the machine without the detour via image data could lead to success in finding very local events. This is not possible with the presented workflow. Another disadvantage of the selected workflow with the use of image data is the high processing time for high-resolution images. Here, it is not the CNN that is the bottleneck, but the conversion of MPM data into image data, which is very computationally intensive and produces large amounts of data.
Further investigations with variation of the post-processing parameters, especially the selected resolution, could also contribute to improvement. However, an advantage of the chosen architecture became apparent when investigating very small data sets. A few images were already sufficient to successfully train a network. In addition, the versatility of the workflow became apparent when analyzing images showing the entire build job. Without having to change the network architecture, images with different resolutions could be processed. This suggests that the integration of image data from other sources, such as camera systems, into the workflow is also very easy. Although the detection of single pores is still too challenging due to their size, it is easily possible to use the presented workflow for the detection of other events.

5 Conclusion and Outlook

In this work the development and investigation of its applicability of a Machine Learning workflow for automatic defect detection for Selective Laser Melting has been presented.

5.1 Conclusion

The elaborated workflow features the design of specific samples with artificial cavities, the preproscessing of the SLM input data, manufacturing and postprocessing of the gathered data, as well as the generation of specific data sets with which a CNN is trained. Additionally, further analysis features like CT and conventional image analysis are featured in the workflow. A CNN was used for object recognition in image data, since this approach is particularly versatile and can draw on a wealth of experience with such architectures in a wide variety of application fields. YOLO, such an object recognition algorithm, was chosen because it allows application in scenarios where real-time detection is required.
This image-driven approach required the processing of the collected data into image data with the highest possible significance. From the presented results it can be concluded that the parameter selection in this step has a very high influence on the quality of the detection results. Furthermore, a great influence of the scan strategy and the layer building time on the MPM data could be demonstrated. This has the particular consequence that the detection of less influential events is significantly more difficult. The influence of the layer build time could be reduced in the future by setting the minimum layer build time higher than the maximum geometry-related layer build time of a build job. However, this would result in significantly higher overall build times and would mean downtimes during which no manufacturing is performed. This in turn would significantly reduce the economic efficiency of the SLM process. To overcome this challenge more research investigating the influence of layer build times is necessary.
The workflow has been successfully used for the detection of geometrically large and small events if the intensity of these events is very high. Thus the basic applicability for the purpose of defect detection can be proven. However, breaking down anomaly detection in MPM data to object detection in image data shows clear limitations when very local events with low intensities are involved, such as the formation of gas pores. The workflow could not be used to classify undetected events with the eye and conventional analysis methods. Furthermore, it was shown that events such as strong gray value increases in cover layers can be detected, but the produced data is not sufficient to generate a precise classifier. Nevertheless, it was possible to show that the simultaneous detection of different events, like cavities and their covers, and their classification is easily possible with the developed workflow.
By examining data sets of different size and variety, it could be shown that diversity is most

crucial for success. This means in particular that when using the workflow, the greatest possible diversity of data should be taken into account. This can be achieved in part through data augmentation, but should also be taken into account in the design and preprocessing steps of samples.
Brief analysis of the manufactured samples using CT showcased the potential of using the gathered data for comparison with the measured MPM-Data. Moreover, it provided useful insights regarding the manufacturing process itself. The results highlighted the difficulties in producing small cavities true to size and shape in components and allowed to judge the quality of such in relation to their size. Like so, it was shown that spherical cavities with diameters below 150 μm are not produced reliably with the given techniques, parameters and materials.
The aim of this thesis to investigate how defects can be detected automatically, using ML algorithms has been achieved by developing and testing a completely new workflow. It has been shown, that artificial designed defects can be detected by solely relying on data gathered by built-in photodiodes with the suggested image-driven concept. This workflow is very easy to customize and all individual tasks can be exchanged or improved. It is designed to be implemented seamlessly into existing SLM pre- and post-processing frameworks, as no additional hardware is needed. Furthermore, the presented workflow allows a use beyond the application of defect detection, as its architecture allows very versatile usage.

5.2 Outlook

This work represents only a first step in the development of an automatic defect detector. The basic concept could be developed and validated with sample data, but an important goal was to create a starting point for further research. Here some impulses shall be presented, how the proposed concept could be further developed in the future. For this purpose, open questions and ideas are divided into four areas: Data, Workflow, SLM process and Machine Learning.

5.2.1 Data

In order to investigate how cavities of different size and shape are detectable in MPM-data, more samples should be manufactured featuring cavities with diameters between 400 μm and 2000 μm. The presented research showed that cover layers of cylindrical cavities with diameters of 2000 μm or more can be detected in principle with the elaborated workflow. However, cover layers of cavities with diameters of 400 μm could neither be detected by analyzing the image data conventionally, not by training a neural network. Therefore the question remains unresolved as to what size artificial defects can be detected by their cover layers. Furthermore, the design of these samples should feature more, but flatter cylindrical cavities to generate more cover layers per sample. A larger number of cover layers can then be used to further investigate the detection of these.
Moreover, the applicability of the workflow for detection of various other features in MPM-data should be examined. As the workflow supports object detection in image data it is

not restricted to the detection of specific events in the data. This means, that events like hotspots, occuring due to component geometry, chosen parameters or changes of environmental parameters could be used for training, resulting in a more generalized network that could detect regions with higher energy input in a build job. A benefit of using a CNN like YOLO is its ability to not only detect objects in an image, but also to put this information into context. It has been shown that it is possible to train CNNs to describe images, as they become more and more able to understand context. This could potentially be used to train a CNN to not only recognize regions of higher intensities, but also analyze potential causes, like geometry, risks, like cracks and even measures to counteract, like adjustment of laser power in this region in following layers.
One further use of the proposed workflow could be the classification of porosities not as individual events, but rather as predicted averaged porosities in a component or a specific region of a component. As discussed in chapter 4.3.1, there is a correlation between average porosity in a sample, volume energy density and the mean intensity in the gathered MPM-data. Manufacturing more samples with varying volume energy density should provide enough data to train a porosity prediction network. Considering the findings in chapter 4.3.2 regarding the influence of the scan strategy and resulting oscillation of the mean intensity, it is advised to average ten layers to account for this effect.
Furthermore, the use of CT-Data could be intensified. Gobert er al. [13] used CT data to analyze produced samples and transferred labels of defects from CT to image data. Using 3D geometry matching, transfering locations and sizes of defects could potentially be automated. Going even further, it would be possible to train a CNN with CT and MPM images at the same time, or successively, first training with CT data and only then training the pretrained network additionally with MPM data of which a smaller amount would be necessary. The CNN is expected to learn certain features, present in both data types. However, this would require basic discoverability of defects, which is yet to be investigated.

5.2.2 Workflow

The workflow should be automated as much as possible to decrease manual work. This means in particular the automation of the labeling process, as it requires a lot of manual work. As introduced, it requires the manual transfer of the dimensions of the geometries into the labeling script for each cavity. This step can be replaced by reading dimensions from universal CAD formats such as STEP automatically. Additionally label positions and sizes should be altered by random margins to prevent overfitting, as investigated in chapter 4.1.2. Furthermore integration of the presented workflow into the existing pre- and postprocessing framework, developed at the Institute for Software Technology should be considered. This would allow to integrate detection of features and events into data analysis and help scientists to better understand processes and their effects as well as gain knowledge about process parameter selection.
Ultimately the goal is to integrate the presented methods into the production process. The real-time ability of YOLO allows to use the CNN in-situ to not only analyze the process after manufacturing, but during production. Possible applications could be rather simple

warning systems, giving a warning if the MPM-data produced in the current layer suggest defects that could potentially harm the machine or process. Moreover, a feedback-loop could be implemented to not only monitor the process, but take appropriate actions, if necessary.

5.2.3 SLM process

To further investigate the influence of the chosen scan strategy, MPM-data of components manufactured with varying scan patterns should be analyzed to compare results. This is expected to help understand and tackle the oscillation of the mean intensity. Already performed examinations of the three manufactured parameter sets suggest that there is a linear relationship between energy input and MPM-data. The suggested research would provide data to investigate this relationship even further and would also allow the consideration of this correlation in data analysis.
Furthermore, there should be investigations how the layer build time influences the MPM-data to be able to account for this parameter in analysis. The examined data of a Parameter Stack in chapter 4.3.1 suggest a great influence of this parameter. However, the extent of alteration of this parameter was very large in the conducted research. Therefore samples should be manufactured whose layer surface and thus layer building time increases or decreases about every 20 layers. Maybe even data of already manufactured components could be analyzed.

5.2.4 Machine Learning

Lastly, the used ML technique should be investigated further. To optimize the CNN parameter studies should be carried out to enhance its performance for the specific use-case of detecting cover layers. Parameters to adjust include the number of filters, which should be adjusted based on the number of classes, and the network input size, in this work at 416 by 416. Moreover, the stride of filters sliding over layers could be manipulated, as well as the number of YOLO layers, as suggested by Bochkovskiy et al. [5].
In this work only one ML algorithm was tested. Therefore in future research the implementation of various ML techniques should be considered. As mentioned before, first the application of a drastically different approach should be tested by implementing a unsupervised learning technique which can be trained with raw machine data, bypassing the intermediate process of image generation and processing. Unsupervised learning technique like clustering are more likely to detect anomalies in data, which can not be detected by the human eye. Eliminating labeling would also reduce manual labor and one source of error. Therefore, the applicability of such algorithms should be investigated and results should be compared to the ones presented in this work.

A Appendix

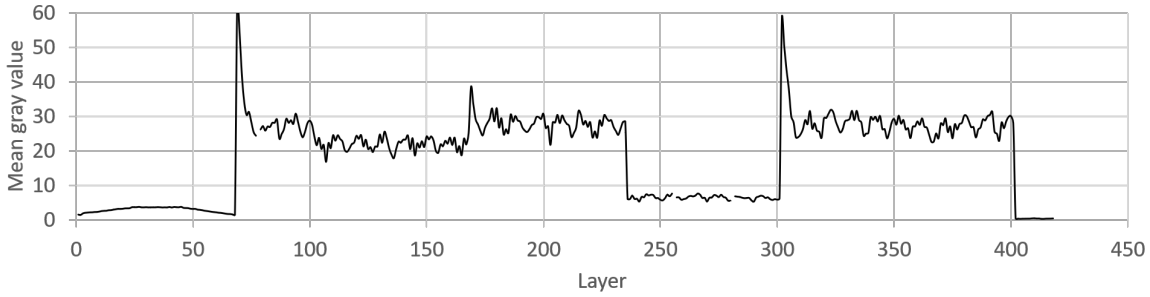

Figure A-1: Mean gray values of all layers of five averaged C_{2000} samples.

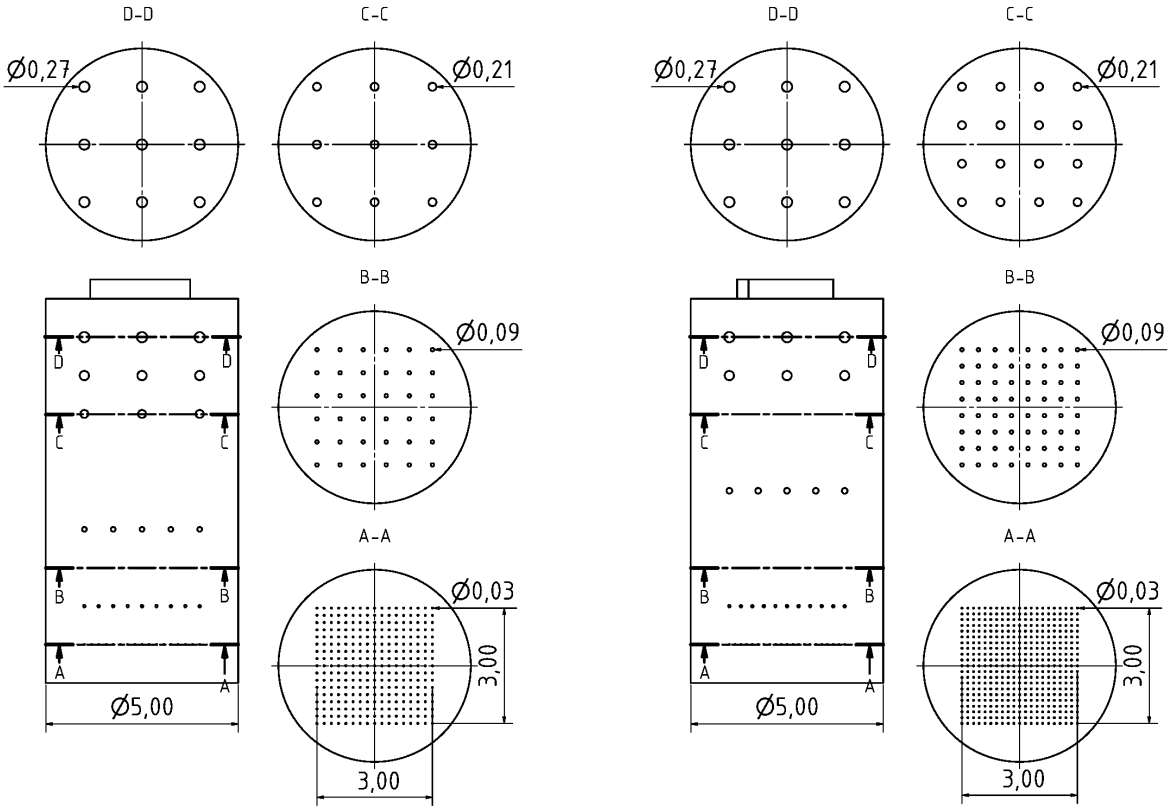

(a) Technical drawing of a sample of type P_2

(b) Technical drawing of a sample of type P_3.

Figure A-2: Technical Drawings of P-Series samples

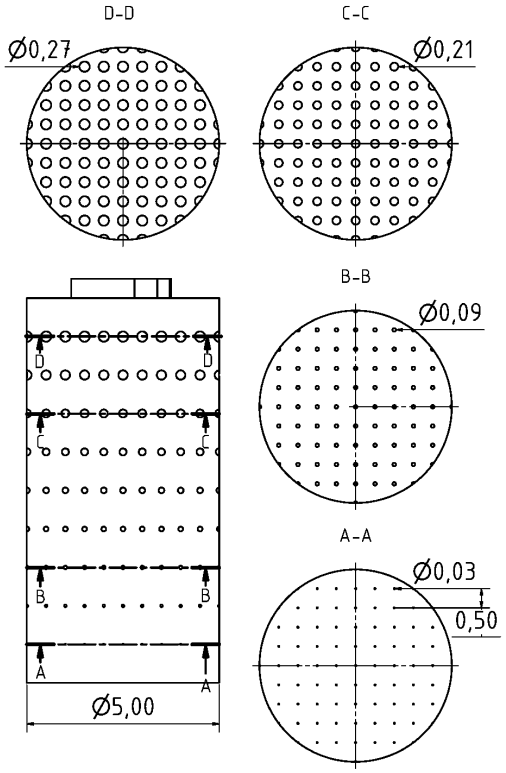

(a) Technical drawing of a sample of type P_{Var}

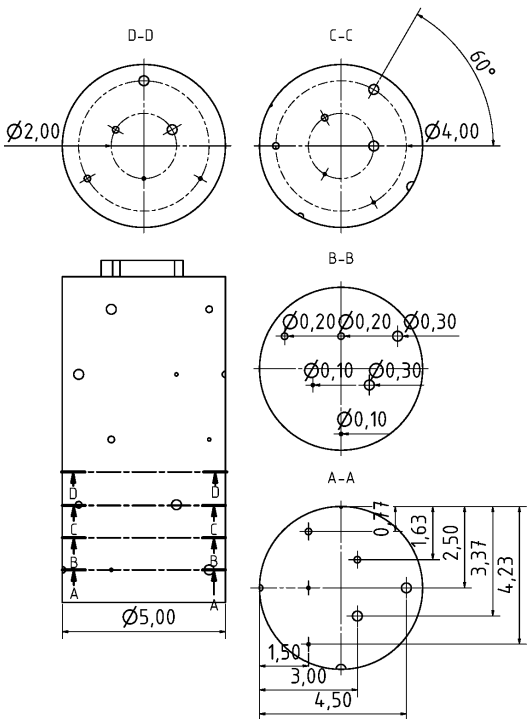

(b) Technical drawing of a sample of type S_1.

Figure A-3: Technical Drawings P_{Var} and S_2 samples

Bibliography

[1] N. T. Aboulkhair et al. “On the precipitation hardening of selective laser melted AlSi10Mg”. In: *Metallurgical and Materials Transactions A* 46.8 (2015), pp. 3337–3341.

[2] N. T. Aboulkhair et al. “Reducing porosity in AlSi10Mg parts processed by selective laser melting”. In: *Additive Manufacturing* 1 (2014), pp. 77–86.

[3] H. Baumgartl et al. “A deep learning-based model for defect detection in laser-powder bed fusion using in-situ thermographic monitoring”. In: *Progress in Additive Manufacturing* (2020), pp. 1–9.

[4] S. Berumen et al. “Quality control of laser-and powder bed-based Additive Manufacturing (AM) technologies”. In: *Physics procedia* 5 (2010), pp. 617–622.

[5] A. Bochkovskiy, C.-Y. Wang, and H.-Y. M. Liao. “YOLOv4: Optimal Speed and Accuracy of Object Detection”. In: *arXiv e-prints*, arXiv:2004.10934 (2020).

[6] S. Clijsters, T. Craeghs, and J.-P. Kruth. “A priori process parameter adjustment for SLM process optimization”. In: *Innovative developments on virtual and physical prototyping* (2012), pp. 553–560.

[7] T. Craeghs et al. “Online quality control of selective laser melting”. In: *Proceedings of the 20th Solid Freeform Fabrication (SFF) symposium, Austin (Texas), 8-10 august*. 2011, pp. 212–226.

[8] J. Davis et al. “Smart manufacturing”. In: *Annual review of chemical and biomolecular engineering* 6 (2015), pp. 141–160.

[9] C. R. Deckard. *Method and apparatus for producing parts by selective sintering*. US Patent 4,863,538. Sept. 1989.

[10] M. Everingham et al. “The 2005 pascal visual object classes challenge”. In: *Machine Learning Challenges Workshop*. Springer. 2005, pp. 117–176.

[11] S. K. Everton et al. “Review of in-situ process monitoring and in-situ metrology for metal additive manufacturing”. In: *Materials & Design* 95 (2016), pp. 431–445.

[12] J. Glasschroeder, E. Prager, and M. F. Zaeh. “Powder-bed-based 3D-printing of function integrated parts”. In: *Rapid Prototyping Journal* (2015).

[13] C. Gobert et al. “Application of supervised machine learning for defect detection during metallic powder bed fusion additive manufacturing using high resolution imaging.” In: *Additive Manufacturing* 21 (2018), pp. 517–528.

[14] H. Gong et al. “Analysis of defect generation in Ti–6Al–4V parts made using powder bed fusion additive manufacturing processes”. In: *Additive Manufacturing* 1 (2014), pp. 87–98.

[15] M. Grasso et al. “In-Process Monitoring of Selective Laser Melting: Spatial Detection of Defects Via Image Data Analysis”. In: *Journal of Manufacturing Science and Engineering* 139.5 (Nov. 2016).

[16] D. Gu et al. “Densification behavior, microstructure evolution, and wear performance of selective laser melting processed commercially pure titanium”. In: *Acta Materialia* 60.9 (2012), pp. 3849–3860.

[17] T. J. Horn and O. L. Harrysson. “Overview of current additive manufacturing technologies and selected applications”. In: *Science progress* 95.3 (2012), pp. 255–282.

[18] G. Kasperovich and J. Hausmann. “Improvement of fatigue resistance and ductility of TiAl6V4 processed by selective laser melting”. In: *Journal of Materials Processing Technology* 220 (2015), pp. 202–214.

[19] G. Kasperovich et al. “Correlation between porosity and processing parameters in TiAl6V4 produced by selective laser melting”. In: *Materials & Design* 105 (2016), pp. 160–170.

[20] M. Khanzadeh et al. “Porosity prediction: Supervised-learning of thermal history for direct laser deposition”. In: *Journal of Manufacturing Systems* 47 (Apr. 2018), pp. 69–82.

[21] O. Kwon et al. “A convolutional neural network for prediction of laser power using melt-pool images in laser powder bed fusion”. In: *IEEE Access* PP (Jan. 2020), pp. 1–1.

[22] C. H. Lampert, M. B. Blaschko, and T. Hofmann. “Beyond sliding windows: Object localization by efficient subwindow search”. In: *2008 IEEE conference on computer vision and pattern recognition*. IEEE. 2008, pp. 1–8.

[23] A. L. Maas, A. Y. Hannun, and A. Y. Ng. “Rectifier nonlinearities improve neural network acoustic models”. In: *Proc. icml*. Vol. 30. 1. 2013, p. 3.

[24] M. Mani et al. “A review on measurement science needs for real-time control of additive manufacturing metal powder bed fusion processes”. In: *International Journal of Production Research* 55.5 (2017), pp. 1400–1418.

[25] W. Meiners. “Direktes selektives Laser-Sintern einkomponentiger metallischer Werkstoffe”. PhD thesis. Aachen: RWTH-Aachen University, 1999.

[26] I. A. Okaro et al. “Automatic fault detection for laser powder-bed fusion using semi-supervised machine learning”. In: *Additive Manufacturing* 27 (May 2019), pp. 42–53.

[27] M. Orme et al. “Topology optimization for additive manufacturing as an enabler for light weight flight hardware”. In: *Designs* 2.4 (2018), p. 51.

[28] C. Panwisawas et al. “On the role of thermal fluid dynamics into the evolution of porosity during selective laser melting”. In: *Scripta Materialia* 105 (2015), pp. 14–17.

[29] C. Qiu, N. J. Adkins, and M. M. Attallah. “Microstructure and tensile properties of selectively laser-melted and of HIPed laser-melted Ti–6Al–4V”. In: *Materials Science and Engineering: A* 578 (2013), pp. 230–239.

[30] O. A. Quintana et al. “Effects of reusing Ti-6Al-4V powder in a selective laser melting additive system operated in an industrial setting”. In: *JOM* 70.9 (2018), pp. 1863–1869.

[31] J. Redmon. *Darknet: Open Source Neural Networks in C*. `http://pjreddie.com/darknet/`. 2013–2016.

[32] J. Redmon et al. “You Only Look Once: Unified, Real-Time Object Detection”. In: *CoRR* abs/1506.02640 (2015). arXiv: `1506.02640`.

[33] P. Rosauer. “Parametrisierung des Selektiven Laserschmelzens von AlSi10Mg für Raumfahrtanwendungen”. 2020.

[34] C. T. Rueden et al. “ImageJ2: ImageJ for the next generation of scientific image data”. In: *BMC bioinformatics* 18.1 (2017), p. 529.

[35] A. L. Samuel. “Some studies in machine learning using the game of checkers”. In: *IBM Journal of research and development* 3.3 (1959), pp. 210–229.

[36] J. Schmidhuber. “Deep learning in neural networks: An overview”. In: *Neural Networks* 61 (2015), pp. 85–117.

[37] S. A. Shevchik et al. “Acoustic emission for in situ quality monitoring in additive manufacturing using spectral convolutional neural networks”. In: *Additive Manufacturing* 21 (2018), pp. 598–604.

[38] J. Spallek and D. Krause. “Process types of customisation and personalisation in design for additive manufacturing applied to vascular models”. In: *Procedia CIRP* 50 (2016), pp. 281–286.

[39] Statista. “Most used 3D printing technologies in 2020”. In: (2020). Retrieved, 25 November 2020.

[40] R. S. Sutton and A. G. Barto. *Reinforcement learning: An introduction*. MIT press, 2018.

[41] C. Wang et al. “Machine learning in additive manufacturing: State-of-the-art and perspectives”. In: *Additive Manufacturing* 36 (2020), p. 101538.

[42] M. Weber, M. Welling, and P. Perona. “Unsupervised learning of models for recognition”. In: *European conference on computer vision*. Springer. 2000, pp. 18–32.

[43] T. Wohlers and T. Gornet. “History of additive manufacturing”. In: *Wohlers report* 24.2014 (2014), p. 118.

[44] T. Wuest et al. “Machine learning in manufacturing: advantages, challenges, and applications”. In: *Production & Manufacturing Research* 4.1 (2016), pp. 23–45.

[45] P. Yadav et al. “In situ monitoring systems of the SLM process: On the need to develop machine learning models for data processing”. In: *Crystals* 10.6 (2020), p. 524.

[46] L. Yang et al. *Additive manufacturing of metals: the technology, materials, design and production*. Springer, 2017.

[47] B. Zhang, Y. Li, and Q. Bai. “Defect formation mechanisms in selective laser melting: a review”. In: *Chinese Journal of Mechanical Engineering* 30.3 (2017), pp. 515–527.

[48] C. Zitelli, P. Folgarait, and A. Di Schino. “Laser powder bed fusion of stainless steel grades: a review”. In: *Metals* 9.7 (2019), p. 731.

Declaration of Originality

„I hereby confirm that I have written the submitted work independently. All passages taken literally or analogously from published or unpublished works of others have been marked as such. All sources and aids that I have used for the work are indicated. The thesis has not been submitted to any other examination authority with the same content or in essential parts.
I am aware that the university reserves the right to check my work for plagiarized content and that the discovery of plagiarized content can lead to the invalidity of the work, the revocation of the degree and exmatriculation.“

Erklärung zur Masterarbeit

„Ich versichere hiermit, die von mir vorgelegte Arbeit selbstständig verfasst zu haben. Alle Stellen, die wörtlich oder sinngemäß aus veröffentlichten oder nicht veröffentlichten Arbeiten anderer entnommen sind, habe ich als entnommen kenntlich gemacht. Sämtliche Quellen und Hilfsmittel, die ich für die Arbeit benutzt habe, sind angegeben. Die Arbeit hat mit gleichem Inhalt bzw. in wesentlichen Teilen noch keiner anderen Prüfungsbehörde vorgelegen.
Mir ist bewusst, dass sich die Hochschule vorbehält, meine Arbeit auf plagiierte Inhalte hin zu überprüfen und dass das Auffinden von plagiierten Inhalten zur Nichtigkeit der Arbeit, zur Aberkennung des Abschlusses und zur Exmatrikulation führen können.“

Place, Date Ort, Datum	Signature Unterschrift